日本磁気学会
ISSN 2432-0250
Journal of the Magnetics Society of Japan
Electronic Journal URL: https://www.jstage.jst.go.jp/browse/msjmag

Vol.49 No.1　2025

# Journal

# JOURNAL OF THE MAGNETICS SOCIETY OF JAPAN

Vol.49 No.1 2025

日本磁気学会

ISSN 2432-0250

HP: http://www.magnetics.jp/ e-mail: msj@bj.wakwak.com

Electronic Journal: http://www.jstage.jst.go.jp/browse/msjmag

# Journal of the Magnetics Society of Japan
## Vol. 49, No. 1

Electronic Journal URL: https://www.jstage.jst.go.jp/browse/msjmag


## CONTENTS




## Board of Directors of The Magnetics Society of Japan

| | |
|---|---|
| **President:** | Y. Takemura |
| **Vice Presidents:** | T. Ono, A. Kikitsu |
| **Directors, General Affairs:** | H. Yuasa, T. Yamada |
| **Directors, Treasurer:** | A. Yamaguchi, S. Murakami |
| **Directors, Planning:** | M. Mizuguchi, Y. Okada |
| **Directors, Editorial:** | S. Yabukami, T. Taniyama |
| **Directors, Public Relations:** | K. Kakizaki, R. Umetsu |
| **Directors, International Affairs:** | H. Kikuchi, Y. Nozaki |
| **Specially Appointed Director, Contents Control & Management:** | K. Nakamura |
| **Specially Appointed Director, Societies & Academic Collaborations:** | A. Saito |
| **Specially Appointed Director, IcAUMS:** | H. Yanagihara |
| **Auditors:** | K. Kobayashi, H. Saito |

Copyright ©2024 by the Magnetics Society of Japan.
This article is licensed under the Creative Commons Attribution International License (CC BY 4.0)
http://creativecommons.org/licenses/by/4.0/



J. Magn. Soc. Jpn., **49**, 1-8 (2025) <Paper>

# Influence of Damping Constant on Writability in Heated-Dot Magnetic Recording

T. Kobayashi, I. Tagawa*, and Y. Nakatani**

Graduate School of Engineering, Mie Univ., *1577 Kurimamachiya-cho, Tsu 514-8507, Japan*

*Electrical and Electronic Engineering, Tohoku Institute of Technology, *35-1 Yagiyama-Kasumicho, Sendai 982-8577, Japan*

**Graduate School of Informatics and Engineering, Univ. of Electro-Communications, *1-5-1 Chofugaoka, Chofu 182-8585, Japan*

We discuss the influence of the damping constant $\alpha$ on writability in heated-dot magnetic recording using our stochastic calculation employing the Néel-Arrhenius model with a Stoner-Wohlfarth dot, since the duration for the non-Néel-Arrhenius type is very short in the writing time and most of the writing time is the Néel-Arrhenius type. The bit error rate is calculated and the result is analyzed using the mean magnetization reversal numbers per unit time $N_+$ and $N_-$ for the magnetization reversal in the direction opposite to the recording direction and in the recording direction, respectively. The writing improves as the $N_+$ value decreases and the $N_-$ value increases. The $N_+$ and $N_-$ values decrease as the $\alpha$ value decreases, since the attempt frequency is approximately proportional to $\alpha$. The writing time when the $N_-$ value is large is rather short compared with the writing time determined by the writing field. Therefore, a magnetization reversal time that is much shorter than the writing time is needed to write data. The $1/N_-$ value represents the stochastic magnetization reversal time under thermal agitation, and the $1/N_-$ value is inversely proportional to $\alpha$. Although the $N_+$ value becomes small, a small $\alpha$ value is disadvantageous to writing.

**Key words:** HDMR, Gilbert damping constant, stochastic calculation, micromagnetic simulation, bit error rate, reversal number, reversal time

## 1. Introduction

Many magnetic recording methods have been proposed to solve the trilemma problem[1] of conventional magnetic recording (CMR) on granular media. These methods include shingled magnetic recording (SMR), microwave-assisted magnetic recording (MAMR), heat-assisted magnetic recording (HAMR), bit patterned media (BPM), heated-dot magnetic recording (HDMR), namely HAMR on BPM, and three-dimensional magnetic recording (3D MR).

Akagi *et al.* reported writability in HDMR[2] and 3D HDMR[3,4] employing micromagnetic simulation. They assumed the medium material to be FePt. However, the anisotropy constant $K_u$ was smaller than that of bulk FePt.

We have discussed the influence of $K_u$ on writability in HDMR[5] employing our stochastic calculation using the Néel-Arrhenius model with a Stoner-Wohlfarth dot. We explained why HDMR with a small $K_u$ exhibits good writability using the mean magnetization reversal number per unit time $N_+$ in the opposite direction to the recording direction and the $N_-$ value in the recording direction during writing. When we choose a small $K_u$ value, the $N_+$ value becomes negligible. Furthermore, the duration where the $N_-$ value is large becomes longer. These are advantageous as regards writability.

A feature of our stochastic calculation is that it is easy to grasp the physical implication of HAMR writing including HDMR.

The magnetization precession, namely the damping constant is a common problem for HAMR and HDMR. We have already discussed the influence of the damping constant on writability for media with relatively small and large anisotropy constants in HAMR[6] employing our stochastic and micromagnetic calculations. However, the discussion lacked the temperature dependence of an attempt frequency, namely the perspective provided by the $N_\pm$ values. Using the $N_\pm$ values, we can understand the magnetization motion during writing in detail.

In this paper, we discuss the influence of the damping constant on writability for a medium with a large anisotropy constant in 4 Tbpsi shingled HDMR, employing our stochastic calculation using the $N_\pm$ values. This condition simplifies the analysis of the writing process, since 1 bit consists of 1 dot for HDMR and erasure-after-write can be ignored for a medium with a large anisotropy constant[5]. We confirm the stochastic calculation result by employing a micromagnetic simulation.

## 2. Calculation Conditions and Method

### 2.1 Dot arrangement and medium structure

Figure 1 shows the dot arrangement and medium structure in 4 Tbpsi HDMR where $D_x$, $D_y$, and $h$ are the dot sizes for the down-track $x$ and cross-track $y$ directions, and the dot height, respectively. The $z$ direction is film normal. The bit length $D_B$ and track width $D_T$ are both 12.7 nm. We assume that the mean dot size $D_m$ and mean dot spacing $\Delta_D$ are the same for

Corresponding author: T. Kobayashi (e-mail: kobayasi @phen.mie-u.ac.jp).

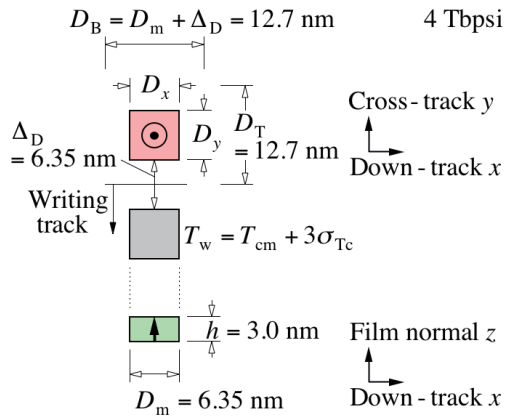


**Fig. 1** Dot arrangement and medium structure.

both the down-track and cross-track directions, namely $D_m = \Delta_D = 6.35$ nm.

There are two cases as regards the dot sizes $D_x$ and $D_y$ depending on the dot manufacturing method. In one, the $D_x$ and $D_y$ sizes are the same, and the $D_x = D_y$ size fluctuates. In the other case, the $D_x$ and $D_y$ sizes fluctuate independently. We examined the $D_x = D_y$ case. We generated a random number $D_x = D_y$ that had a log-normal distribution with a standard deviation $\sigma_D$. We used a $\sigma_D/D_m$ value of 15 %.

### 2.2 Temperature profile and writing field

The writing temperature $T_w$ for the dot was assumed to be

$$T_w = T_{cm} + 3\sigma_{Tc}, \quad (1)$$

as shown in Fig. 1, after taking account of the Curie temperature $T_c$ variation, where $T_{cm}$ and $\sigma_{Tc}$ are the mean Curie temperature and the standard deviation of $T_{cm}$, respectively. The $T_c$ distribution was assumed to be normal. Based on this assumption, 99.9 % of the dots in the writing track are heated to above their $T_c$ values during the writing period. We used $T_{cm}$ and $\sigma_{Tc}/T_{cm}$ values of 750 K and 2 %, respectively.

For simplicity, we used a thermal gradient $\partial T/\partial y$ of 14 K/nm in the cross-track direction and assumed it to be constant anywhere for adjacent track interference (ATI). A constant thermal gradient $\partial T/\partial x$ of 14 K/nm in the down-track direction was also used for writability.

The writing field $H_w$ was assumed to be spatially uniform, the direction to be perpendicular to the medium plane, and the rise time to be zero.

### 2.3 Magnetic properties

The temperature $T$ dependence of the medium magnetization $M_s$ was calculated by employing mean field analysis[7] for $(Fe_{0.5}Pt_{0.5})_{1-c}Cu_c$, and that of the $K_u$ value was assumed to be proportional to $M_s^2$[8]. $M_s(T_c = 770\ \mathrm{K}, T = 300\ \mathrm{K}) = 1000$ emu/cm$^3$ was assumed for FePt. Based on this assumption, the $M_s$ value can be calculated for all values of $T_c$ and $T$.

Since each dot has a $T_c$ variation, the $T_c$ value of each dot was adjusted by changing the Cu composition $c$ for $(Fe_{0.5}Pt_{0.5})_{1-c}Cu_c$.

**Table 1** Calculation conditions.

| | |
|---|---|
| Recording density (Tbpsi) | 4 |
| Bit length $D_B$ (nm) | 12.7 |
| Track width $D_T$ (nm) | 12.7 |
| Mean dot size $D_m$ (nm) | 6.35 |
| Standard deviation $\sigma_D / D_m$ (%) | 15 |
| Dot height $h$ (nm) | 3.0 |
| Mean dot spacing $\Delta_D$ (nm) | 6.35 |
| Mean Curie temperature $T_{cm}$ (K) | 750 |
| Standard deviation $\sigma_{Tc} / T_{cm}$ (%) | 2 |
| Thermal gradient $\partial T / \partial x$ (K / nm) | 14 |
| Linear velocity (m / s) | 10 |
| Storage temperature (K) for 10 years of archiving | 350 |
| Thermal gradient $\partial T / \partial y$ (K / nm) for ATI | 14 |
| Exposure field (kOe) for ATI | 10 |
| Exposure time (ns) for ATI | 1 |

We used a $K_u$ value of 51 Merg/cm$^3$ and an anisotropy field $H_k$ of 107 kOe at a readout temperature of 330 K.

When we choose an $h$ value, 10 years of archiving, ATI, and writability must be dealt with simultaneously, since they are in a trade-off relationship. The calculation conditions are summarized in Table 1. We assumed the storage temperature to be 350 K for 10 years of archiving, for which we took a certain margin into account. We used an exposure field of 10 kOe and a time of 1 ns for ATI. We fixed the $h$ value at 3.0 nm, taking account of 10 years of archiving and ATI. The limiting factor is 10 years of archiving and the damping constant has little effect on 10 years of archiving[9]. The linear velocity $v$ was 10 m/s.

### 2.4 Stochastic calculation method

The information stability for 10 years of archiving has been discussed employing the Néel-Arrhenius model with a Stoner-Wohlfarth grain or dot[1]. The attempt period $1/f_\alpha$ has a value of picoseconds for FePt in HAMR. Since the magnetization direction attempts to reverse with a certain probability at each attempt period, the information stability for 10 years of archiving is extrapolated as a stack of phenomena in picoseconds. Therefore, the Néel-Arrhenius model is valid for any time from the order of a picosecond to more than 10 years. The Néel-Arrhenius model is also valid on condition that the writing field is smaller than the anisotropy field of the recording media.

Figure 2 shows (a) the temperature dependence of $K_u$ and (b) the time dependence of the effective anisotropy field $H_{keff}$ for a medium with $T_{cm}$, which was calculated from Eq. (11) described below. The medium temperature is also shown. At a time of zero, the medium temperature is assumed to be $T_{cm}$ and the $H_w$ direction changes

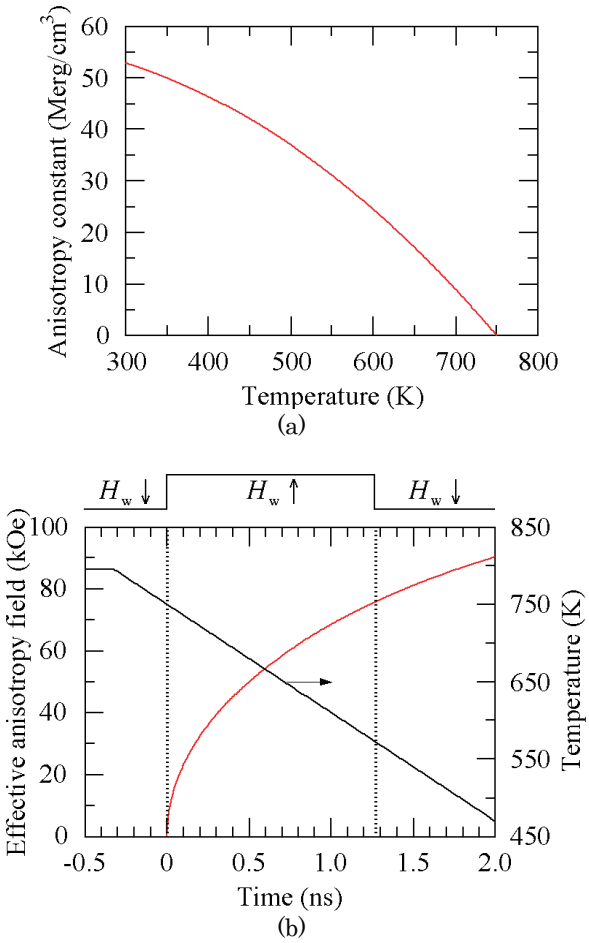


**Fig. 2** (a) temperature dependence of anisotropy constant $K_u$ and (b) time dependence of effective anisotropy field $H_{keff}$ and medium temperature.

from downward to upward, and at a time of 1.27 ns it changes from upward to downward. The writing time defined by $H_w$, namely the field writing time is 1.27 ns. The time is advanced by $\sigma_{Tc}/((\partial T/\partial x)\cdot v)$ for a medium with $T_{cm}+\sigma_{Tc}$ and delayed for a medium with $T_{cm}-\sigma_{Tc}$. When $|H_w| > H_{keff}$, the magnetization reversal is the non-Néel-Arrhenius type. The duration for the non-Néel-Arrhenius type is very short, and most of the field writing time is the Néel-Arrhenius type where $|H_w| < H_{keff}$. In HAMR including HDMR, stochastic magnetization reversal under thermal agitation is dominant even for writability. Therefore, we have been applying the Néel-Arrhenius model to phenomena with a short time and examined ATI[9] and writability[5].

The mean magnetization reversal number per unit time $N$ is expressed as

$$N = f_\alpha \exp(-K_\beta), \tag{2}$$

employing the Néel-Arrhenius model with a Stoner-Wohlfarth grain or dot, where $f_\alpha$ is the attempt frequency[10] and $K_\beta$ is the thermal stability factor. The $f_\alpha$ value gives an attempt number per unit time for magnetization reversal, and the Boltzmann factor $\exp(-K_\beta)$ is interpreted as the probability of magnetization reversal.

When the $|H_w|$ value is less than $H_k$, $f_\alpha \equiv f_{\alpha+}$, $K_\beta \equiv K_{\beta+}$, and $N \equiv N_+$ are given by

$$f_{\alpha+} = \frac{\gamma\alpha}{1+\alpha^2}\sqrt{\frac{M_s H_k^3 V}{2\pi kT}}\left(1-\left(\frac{|H_w|}{H_k}\right)^2\right)\left(1+\frac{|H_w|}{H_k}\right), \tag{3}$$

$$K_{\beta+} = \frac{K_u V}{kT}\left(1+\frac{|H_w|}{H_k}\right)^2, \text{ and} \tag{4}$$

$$N_+ = f_{\alpha+}\exp(-K_{\beta+}), \tag{5}$$

respectively, for magnetization reversal in the opposite direction to the recording direction, where $\gamma$, $\alpha$, $V$, and $k$ are the gyromagnetic ratio, Gilbert damping constant, dot volume $V = D_x D_y \times h$, and Boltzmann constant, respectively. We used a $\gamma$ value of $1.76\times10^7$ rad s$^{-1}$ Oe$^{-1}$. For magnetization reversal in the recording direction, $f_\alpha \equiv f_{\alpha-}$, $K_\beta \equiv K_{\beta-}$, and $N \equiv N_-$ are given by

$$f_{\alpha-} = \frac{\gamma\alpha}{1+\alpha^2}\sqrt{\frac{M_s H_k^3 V}{2\pi kT}}\left(1-\left(\frac{|H_w|}{H_k}\right)^2\right)\left(1-\frac{|H_w|}{H_k}\right), \tag{6}$$

$$K_{\beta-} = \frac{K_u V}{kT}\left(1-\frac{|H_w|}{H_k}\right)^2, \text{ and} \tag{7}$$

$$N_- = f_{\alpha-}\exp(-K_{\beta-}), \tag{8}$$

respectively.

In our stochastic calculation, we used the effective anisotropy constant $K_{ueff}$ instead of $K_u$ and the effective anisotropy field $H_{keff}$ instead of $H_k$, taking account of the shape anisotropy[11], as

$$K_{ueff} = K_u + \frac{(4\pi-3N_z)M_s^2}{4}, \tag{9}$$

$$N_z = 8\arctan\left(\frac{D_x D_y}{h\sqrt{D_x^2+D_y^2+h^2}}\right), \text{ and} \tag{10}$$

$$H_{keff} = \frac{2K_{ueff}}{M_s}. \tag{11}$$

The magnetostatic field from surrounding dots was ignored.

When calculating the information stability for 10 years of archiving ($|H_w| = 0$) or ATI, we used Eqs. (6) - (8) modified by Eqs. (9) - (11), since the $H_{keff}$ value is of course much larger than $|H_w|$. Although there is a period where $H_{keff} < |H_w|$ during writing, the duration is much short as shown in Fig. 2 (b). The factor $\sqrt{M_s H_k^3/T}$ in Eqs. (3) and (6) has a strong impact on the temperature dependence of $f_{\alpha\pm}$, and $(1-(|H_w|/H_k)^2)(1\pm|H_w|/H_k)$ is a weakly impacting factor since the $H_k$ value is considerably larger than $|H_w|$ for most of the writing time. Although the $\sqrt{M_s H_k^3/T}$ value becomes zero at $T_c$, $(1-(|H_w|/H_k)^2)(1\pm|H_w|/H_k)$ reaches zero at a temperature where $H_k = |H_w|$. We employed the Néel-Arrhenius model for the entire field writing time. To

achieve this, we extended the $f_{\alpha\pm}$ formula to $T_c$ as

$$f_{\alpha\pm} = \frac{\gamma\alpha}{1+\alpha^2}\sqrt{\frac{M_s H_{keff}^3 V}{2\pi kT}}\left(1-\left(\frac{|H_w|}{H_{const}}\right)^2\right)\left(1\pm\frac{|H_w|}{H_{const}}\right), \quad (12)$$

so that the $f_{\alpha\pm}$ value becomes zero at $T_c$ where the positive and negative signs are in the same order. $H_{const}$ in Eq. (12) is a fitting parameter for Eqs. (3) and (6) and we used a $H_{const}$ value of 60 kOe. When $|H_w| > H_{keff}$, we assumed that

$$K_{\beta-} = 0. \quad (13)$$

The calculation procedure for the writing field dependence of the bit error rate (bER), namely writability, is described below. The dot temperature fell with time from $T_c$ according to $\partial T/\partial x$ and $v$. The attempt times were calculated using $f_{\alpha\pm}$. The probabilities $\exp(-K_{\beta\pm})$ were calculated for every attempt time. The magnetization direction was determined by the Monte Carlo method for every attempt time. Then the bER value was obtained. The calculation detail has already been reported[12].

The bER in this paper is useful only for comparisons.

## 3. Calculation Results

### 3.1 Writing field dependence of bit error rate

Figure 3 (a) shows the writing field $|H_w|$ dependence of bER calculated employing our stochastic calculation. The bER value increases as the $\alpha$ value decreases.

We confirmed the result in Fig. 3 (a) by employing a micromagnetic simulation in which we solved the Landau-Lifshitz-Gilbert (LLG) equation. The LLG calculation method has already been reported in detail[6]. Figure 3 (b) shows the $|H_w|$ dependence of the signal to noise ratio (SNR) calculated employing a micromagnetic simulation, and Fig. 3 (c) shows the bER value in Fig. 3 (a) as a function of the SNR value in Fig. 3 (b). A good correlation can be seen between them. Therefore, our stochastic calculation in Fig. 3 (a) can almost entirely explain the result of the micromagnetic simulation in Fig. 3 (b).

We first discuss this result in terms of the attempt frequency in the Néel-Arrhenius model and the magnetization reversal time constant in the LLG equation.

Since the $\alpha$ value is considered to be smaller than 0.1, $f_{\alpha\pm}$ is almost proportional to $\alpha$ as shown in Eq. (12) since $\alpha/(1+\alpha^2) \approx \alpha$. This means that the attempt number for the magnetization reversal in the recording direction becomes smaller as the $\alpha$ value decreases. As a result, the bER value increases as the $\alpha$ value decreases.

On the other hand, the LLG equation can be solved for a single domain particle. When the initial magnetization and field directions are the $z$ and $-z$ directions, respectively, and the magnetization direction is expressed in a polar coordinate, the magnetization

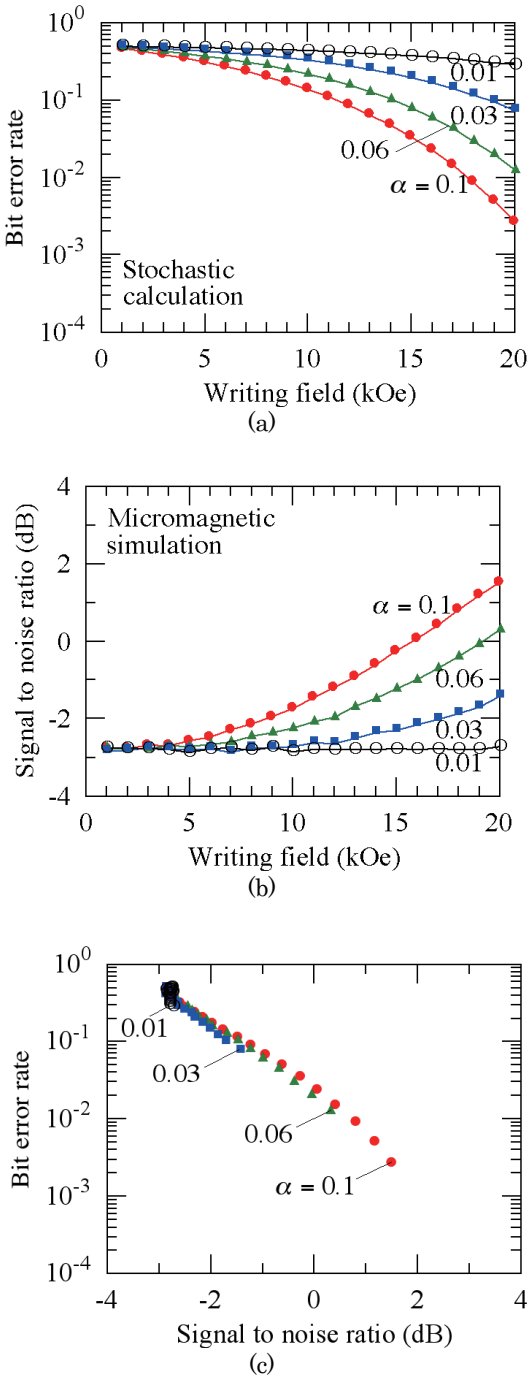


**Fig. 3** Writing field $|H_w|$ dependence of (a) bit error rate (bER) calculated employing our stochastic calculation and (b) signal to noise ratio (SNR) calculated employing a micromagnetic simulation for various $\alpha$ values. (c) The bER value in (a) as a function of the SNR value in (b).

motion is given by

$$\phi = \omega t + \phi_0, \text{ and} \quad (14)$$

$$\theta = 2\arctan\left(\tan\left(\frac{\theta_0}{2}\right)\exp\left(-\frac{t}{\tau}\right)\right), \quad (15)$$

as a function of time $t$ where $\phi$ and $\theta$ are the azimuth

and polar angles, respectively[13]. $\phi_0$ and $\theta_0$ are the initial values at $t = 0$. $\omega$ represents the angular frequency when it is precessing around the field $H$, $\tau$ represents the magnetization reversal time constant in the field direction, and those are given by

$$\omega = \frac{\gamma H}{1+\alpha^2}, \text{ and} \tag{16}$$

$$\tau = \frac{1}{\alpha\omega} = \frac{1+\alpha^2}{\alpha} \cdot \frac{1}{\gamma H}. \tag{17}$$

Equation (17) includes a factor of $(1+\alpha^2)/\alpha \approx 1/\alpha$. This means that the magnetization reversal time becomes longer as the $\alpha$ value decreases. If the magnetization reversal time is too long compared with the writing time, many errors occur. As a result, the bER value increases as the $\alpha$ value decreases.

### 3.2 $N_+$ value and magnetization motion

Next, we discuss the $N_+$ value, which is the mean magnetization reversal number per unit time in the opposite direction to the recording direction, and the corresponding magnetization motion.

The $N_+ = f_{\alpha+} \exp(-K_{\beta+})$ value as a function of time is shown in Fig. 4 for various $\alpha$ values where $|H_w|$ = 10 kOe. As the $N_+$ value decreases, the writing improves, and the $N_+$ value decreases as the $\alpha$ value decreases since the $f_{\alpha+}$ value is proportional to $\alpha/(1+\alpha^2) \approx \alpha$.

We also confirmed the meaning of $N_+$ in Fig. 4 by employing a micromagnetic simulator, EXAMAG LLG (Fujitsu Ltd.)[14], in which the Landau-Lifshitz-Gilbert (LLG) equation is solved by the finite-element method. We added the equivalent field for the energy of the thermal agitation. The calculation step time was $10^{-16}$ s. We focused on the magnetization motion at 0.070 ns in Fig. 4, at which the $N_-$ value for $\alpha$ = 0.1 exhibits its maximum value as shown later in Fig. 6, and the temperature is 740 K. Figure 5 shows the time dependence of the magnetization $z$ component $M_z/M_s$, which means the magnetization motion as a function of time. The initial magnetization and writing field directions are the $-z$ and $z$ directions, respectively. The dot size and magnetic property in Fig. 4 were the same as those in Fig. 5. The calculation temperature was constant at 740 K where $|H_w|$ = 10 kOe and $H_{keff}$ = 19 kOe.

Since the $N_+$(740 K) value is 0.26 ns$^{-1}$ for $\alpha$ = 0.1, we can expect there to be 0.26 mean magnetization reversals in the opposite direction to the recording direction within 1 ns as shown in Fig. 4. As expected, several magnetization reversals can be observed within

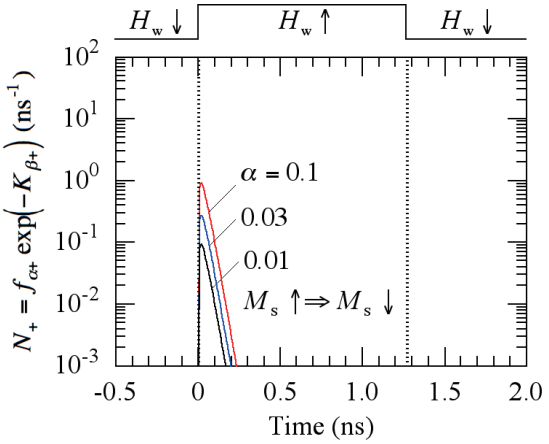


**Fig. 4** Mean magnetization reversal number per nanosecond $N_+ = f_{\alpha+} \exp(-K_{\beta+})$ as a function of time for various $\alpha$ values where $|H_w|$ = 10 kOe.

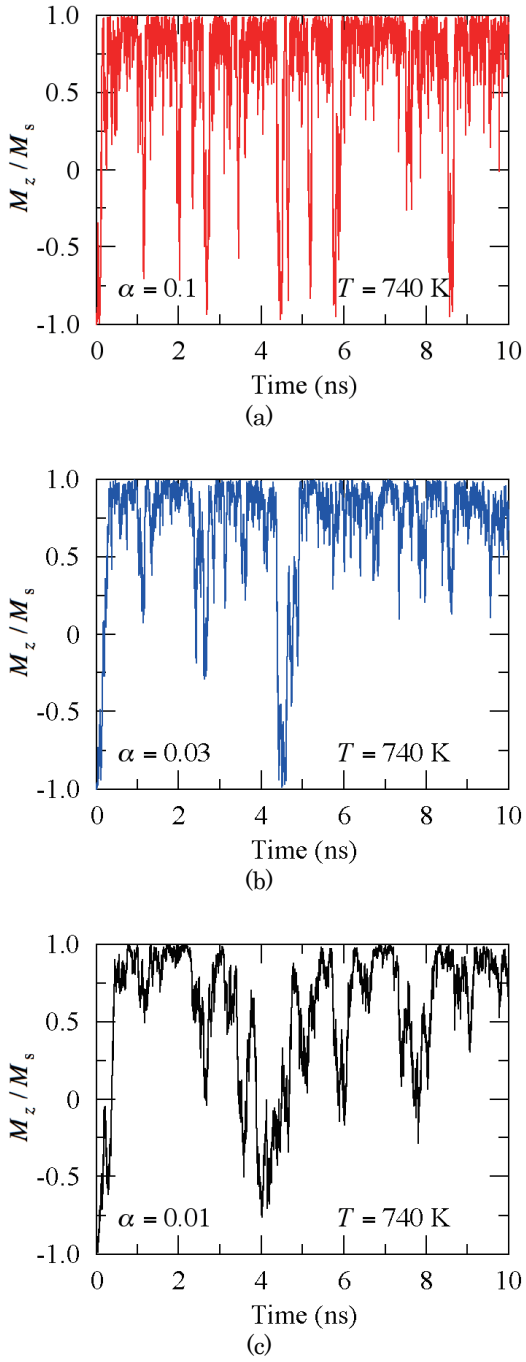


**Fig. 5** Time dependence of magnetization $z$ component $M_z/M_s$ at 740 K (0.070 ns) for (a) $\alpha$ = 0.1[5], (b) $\alpha$ = 0.03, and (c) $\alpha$ = 0.01 where $|H_w|$ = 10 kOe and $H_{keff}$ = 19 kOe.

10 ns as shown in Fig. 5 (a), as already reported[5]. If we employ a definition stating that the magnetization is reversed when the $M_z/M_s$ value falls below than $-0.9$, the magnetization reversal number is 4 times for the example in Fig. 5 (a). This means that there is a situation where the magnetization reverses in the opposite direction to the recording direction. When (b) $\alpha = 0.03$, it is expected that there will be 0.78 mean magnetization reversals in the opposite direction to the recording direction within 10 ns since the $N_+(740\,\mathrm{K})$ value is 0.078 ns$^{-1}$. And one magnetization reversal can be seen in Fig. 5 (b). For (c) $\alpha = 0.01$, the $N_+(740\,\mathrm{K})$ value is 0.026 ns$^{-1}$, and the $M_z/M_s$ value does not reach less than $-0.9$ within 10 ns for this example as shown in Fig. 5 (c).

The stochastic calculation result in terms of the $N_+$ value is consistent with that employing a micromagnetic simulation.

### 3.3 $N_-$ value and magnetization motion

Finally, we discuss the $N_-$ value and corresponding magnetization motion.

The $N_-$ (ns$^{-1}$) value also decreases as the $\alpha$ value decreases as shown in Fig. 6. This means that the mean magnetization reversal number per nanosecond in the recording direction decreases as the $\alpha$ value decreases. The $N_- = f_{\alpha-}\exp(-K_{\beta-})$ value shows the maximum, since the $f_{\alpha-}$ value increases and the $\exp(-K_{\beta-})$ value decreases rapidly as the temperature decreases[5].

We also focused on the magnetization motion at 0.070 ns in Fig. 6. Since the magnetization motion fluctuates with thermal energy, we calculated it using six different random seeds for $\alpha = 0.1$ as shown in Fig. 7 (a). In one case, the magnetization reverses rapidly, and in another case, slowly after time 0. Figure 7 (b) shows the mean magnetization $< M_z >/M_s$ as a function of time for six different random seeds. The $< M_z >/M_s$ reversal time defined by the time for $< M_z >/M_s = 0$ is 0.094 ns, which can be compared to a $1/N_-(740\,\mathrm{K})$ value of 0.073 ns.

The writing time determined by the medium, where the $N_- = f_{\alpha-}\exp(-K_{\beta-})$ value is large, is rather short compared with the field writing time as shown in Fig. 6, since the $\exp(-K_{\beta-})$ value decreases rapidly with time.

Although the temperature was constant for the calculation in Fig. 7, the temperature decreases with time during writing as shown in Fig. 2. For example, at a time of 0.59 ns, which corresponds to a temperature of

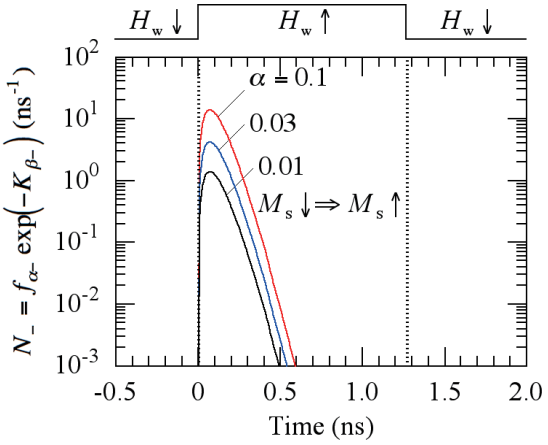


**Fig. 6** Mean magnetization reversal number per nanosecond $N_- = f_{\alpha-}\exp(-K_{\beta-})$ as a function of time for various $\alpha$ values where $|H_w| = 10$ kOe.

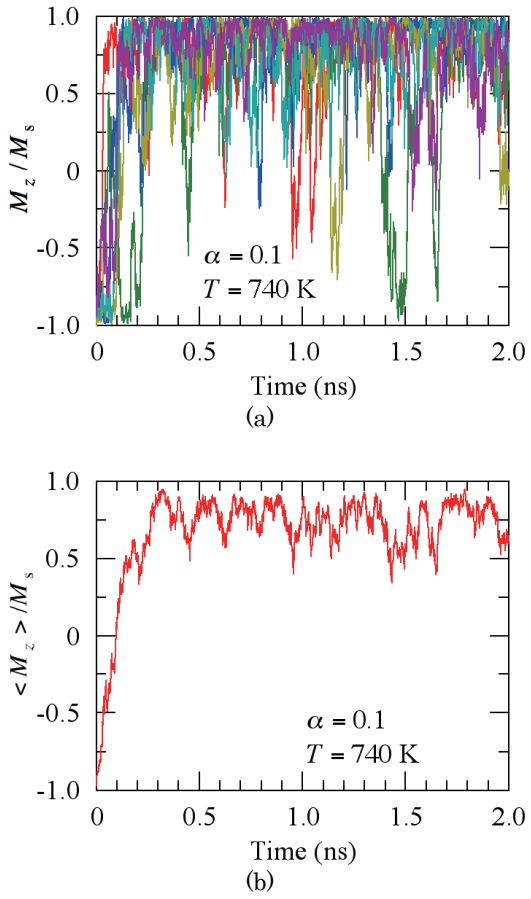


**Fig. 7** (a) Time dependence of magnetization $z$ component $M_z/M_s$ calculated using six different random seeds at 740 K (0.070 ns) for $\alpha = 0.1$ where $|H_w| = 10$ kOe and $H_{keff} = 19$ kOe. (b) Mean magnetization $< M_z >/M_s$ as a function of time.

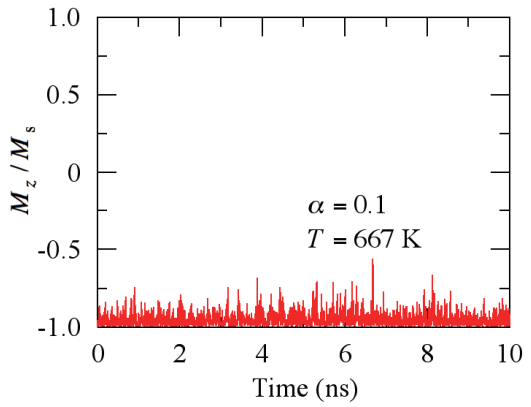


**Fig. 8** Time dependence of magnetization $z$ component $M_z/M_s$ at 667 K (0.59 ns) for $\alpha = 0.1$ where $|H_w| = 10$ kOe and $H_{keff} = 54$ kOe.

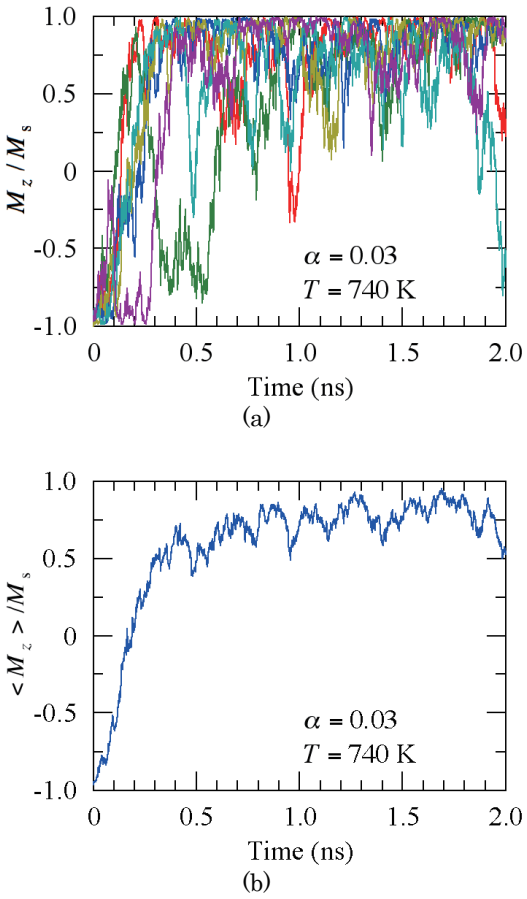


**Fig. 9** (a) Time dependence of magnetization $z$ component $M_z/M_s$ calculated using six different random seeds at 740 K (0.070 ns) for $\alpha$ = 0.03 where $|H_w|$ = 10 kOe and $H_{keff}$ = 19 kOe. (b) Mean magnetization $< M_z >/M_s$ as a function of time.

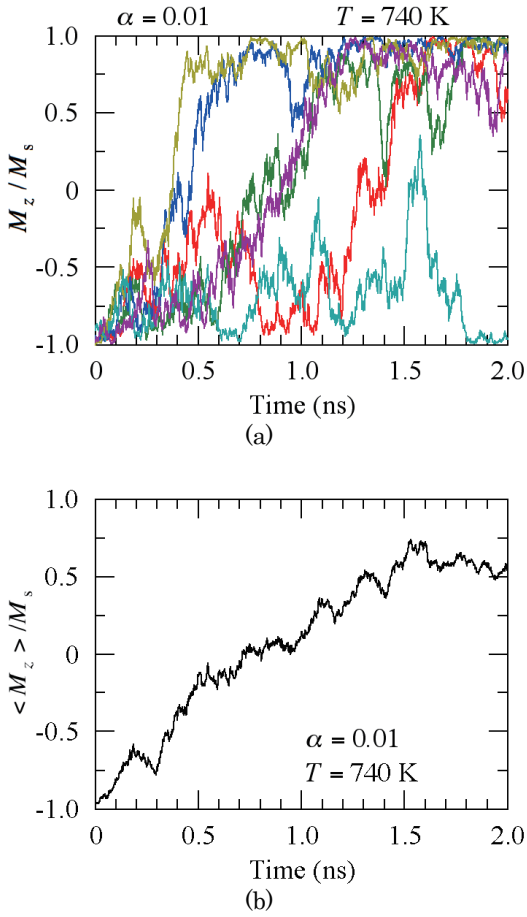


**Fig. 10** (a) Time dependence of magnetization $z$ component $M_z/M_s$ calculated using six different random seeds at 740 K (0.070 ns) for $\alpha$ = 0.01 where $|H_w|$ = 10 kOe and $H_{keff}$ = 19 kOe. (b) Mean magnetization $< M_z >/M_s$ as a function of time.

667 K, the $N_-$ value is about $10^{-3}$ times per nanosecond as shown in Fig. 6. This means that data can no longer be written, and this is confirmed in Fig. 8. The magnetization does not reverse and maintains its initial direction for 10 ns with this example. Therefore, to write data we need a magnetization reversal time much shorter than the field writing time of 1.27 ns.

When $\alpha$ = 0.03, the $< M_z >/M_s$ reversal time is 0.19 ns as shown in Fig. 9 (b), which is comparable to the $1/N_-(740\ \mathrm{K})$ value of 0.24 ns. The $< M_z >/M_s$ reversal time becomes longer than that for $\alpha$ = 0.1.

For $\alpha$ = 0.01, there is one case where no magnetization reversal occurs even within 2 ns for this example as shown in Fig. 10 (a). The $< M_z >/M_s$ reversal time is long at 0.71 ns as shown in Fig. 10 (b), which is comparable to the $1/N_-(740\ \mathrm{K})$ value of 0.72 ns. The $< M_z >/M_s$ reversal time of 0.71 ns is too long for writing with reference to Fig. 6, namely, data can no longer be written. This is disadvantageous to writing.

The $1/N_-$ value is inversely proportional to $\alpha$. The $\tau$ value is also inversely proportional to $\alpha$ as mentioned above. Furthermore, the $H$ value in Eq. (17) includes the equivalent field for the energy of the thermal agitation, and the standard deviation of the equivalent

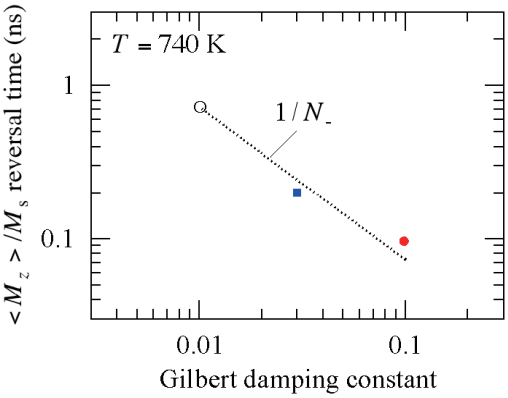


**Fig. 11** Mean magnetization $< M_z >/M_s$ reversal time as a function of Gilbert damping constant.

field is proportional to $\sqrt{\alpha}$. Figure 11 shows the $< M_z >/M_s$ reversal time as a function of $\alpha$. The $1/N_-$ value is also shown. The $< M_z >/M_s$ reversal time and the $1/N_-$ value are almost the same and inversely proportional to $\alpha$. Therefore, the $1/N_-$ value represents the stochastic magnetization reversal time under thermal agitation.

Many calculations are needed to find the mean value

in a micromagnetic simulation. However, in our stochastic calculation, the mean value can be found with one simple calculation of the $N_{\pm}$ values, and therefore, the calculation time is short.

Overall, although the $N_{+}$ value becomes small as shown in Fig. 4, a small $\alpha$ value is disadvantageous to writing as shown in Fig. 3 since the $1/N_{-}$ time becomes long.

## 4. Conclusions

We examined the influence of the damping constant $\alpha$ on writability in 4 Tbpsi shingled heated-dot magnetic recording, using our stochastic calculation. We confirmed the result of this calculation by employing a micromagnetic simulation.

The bit error rate was calculated and the result was analyzed using the mean magnetization reversal numbers per unit time $N_{+}$ and $N_{-}$ for magnetization reversal in the opposite direction to the recording direction and in the recording direction, respectively. The writing improved as the $N_{+}$ and $N_{-}$ values decreased and increased, respectively. Since the $\alpha$ value is considered to be smaller than 0.1, the $N_{+}$ and $N_{-}$ values decreased as the $\alpha$ value decreased.

The writing time where the $N_{-}$ value is large is rather short compared with the field writing time. Therefore, the magnetization reversal time must be much shorter than the field writing time to write data. The $1/N_{-}$ value represents the stochastic magnetization reversal time under thermal agitation, and the $1/N_{-}$ value is inversely proportional to $\alpha$. Although the $N_{+}$ value becomes small, a small $\alpha$ value is disadvantageous to writing since the $1/N_{-}$ time becomes long. As a result, when the anisotropy constant is large, the bit error rate increases as the $\alpha$ value decreases.

The stochastic calculation results are consistent with those obtained with a micromagnetic simulation.

**Acknowledgement** We acknowledge the support of the Advanced Storage Research Consortium (ASRC), Japan.

## References

1) S. H. Charap, P. -L. Lu, and Y. He: *IEEE Trans. Magn.*, **33**, 978 (1997).
2) F. Akagi, M. Mukoh, M. Mochizuki, J. Ushiyama, T. Matsumoto, and H. Miyamoto: *J. Magn. Magn. Mater.*, **324**, 309 (2012).
3) F. Akagi, Y. Sakamoto, and N. Matsushima: 2021 IEEE International Magnetic Conference (INTERMAG), 2100043 (2021). DOI: 10.1109/INTERMAG42984.2021.9580007
4) K. Maeda and F. Akagi: *T. Magn. Soc. Jpn.* (Special Issues) (in Japanese), **7**, 1 (2023).
5) T. Kobayashi, Y. Nakatani, and I. Tagawa: *J. Magn. Soc. Jpn.*, **48**, 81 (2024).
6) T. Kobayashi, Y. Nakatani, F. Inukai, K. Enomoto, and Y. Fujiwara: *J. Magn. Soc. Jpn.*, **41**, 52 (2017).
7) M. Mansuripur and M. F. Ruane: *IEEE Trans. Magn.*, **MAG-22**, 33 (1986).
8) J. -U. Thiele, K. R. Coffey, M. F. Toney, J. A. Hedstrom, and A. J. Kellock: *J. Appl. Phys.*, **91**, 6595 (2002).
9) T. Kobayashi and I. Tagawa: *J. Magn. Soc. Jpn.*, **48**, 40 (2024).
10) E. D. Boerner and H. N. Bertram: *IEEE Trans. Magn.*, **34**, 1678 (1998).
11) T. Kobayashi and I. Tagawa: *J. Magn. Soc. Jpn.*, **47**, 128 (2023).
12) T. Kobayashi, Y. Nakatani, and Y. Fujiwara: *J. Magn. Soc. Jpn.*, **42**, 110 (2018).
13) S. Uchiyama and M. Masuda: *Magnetic Materials* (in Japanese), p. 126 (Corona Publishing Co., Tokyo, 1980).
14) Fujitsu Release: *New Version of EXAMAG LLG Simulator*, https://www.fujitsu.com/global/about/resources/news/press-releases/2015/0324-01.html (2015).

**Received Jul. 20, 2024; Accepted Oct. 4, 2024**

Copyright ©2024 by the Magnetics Society of Japan.
This article is licensed under the Creative Commons Attribution International License (CC BY 4.0)
http://creativecommons.org/licenses/by/4.0/



J. Magn. Soc. Jpn., **49**, 9-12 (2025) <Letter>

# Non-destructive readout method for 3D magnetic memory

Heechan Jang[1], Feifan Ye[1], Yoichi Shiota[1,2], Shutaro Karube[1,2], Ryusuke Hisatomi[1,2], and Teruo Ono[1,2]

[1]Institute for Chemical Research, Kyoto University, *Gokasho, Uji, Kyoto 611-0011, Japan*

[2]Center for Spintronics Research Network, Kyoto University, *Gokasho, Uji, Kyoto 611-0011, Japan*

Recently 3D magnetic memory using artificial ferromagnets has been proposed as a high performance memory solution. However, the existing method for reading information from this device is destructive. Here, we propose a novel nondestructive readout method for 3D magnetic memory, leveraging the magnetization dynamics induced by the spin transfer torque. We show that 16 different identifications in a 4-bit memory are possible by simply reading out the magnetization dynamics of the topmost bit layer of 3D magnetic memory with a magnetic tunnel junction. This advancement paves the way for more reliable 3D magnetic memory technologies.

**Keywords:** domain wall motion memory, non-destructive readout, spin-transfer torque

## 1. Introduction

Magnetic memory using current-driven magnetic domain wall (DW) motion[1-6], such as race-track memory proposed by IBM[7], is expected to be an inexpensive, high-speed, and large-capacity memory. In addition, there is no risk of data crash because there are no moving parts like hard disks. However, there are several issues that need to be resolved to realize DW memory. The first is the control of DW position. Precise control of DW position is indispensable. Otherwise DWs may collide with each other and disappear, and data may even be lost. The current method of controlling the DW position is to fabricate artificial pinning sites in nanowires[8-11], but this method requires complex nanofabrication. The second is to reduce the DW driving current for low-power devices. Although many studies have been conducted since the proposal of the race-track memory, such as the use of perpendicularly magnetized films[9-14], DW motion by spin-orbit torque[15-17], and the use of synthetic antiferromagnets[18], the compatibility of thermal stability of DWs and low-current drive is still a major issue. The third is the DW width. A high-density DW memory can be realized if the DW width is narrower, but the DW width is determined by the material parameters such as the exchange interaction and the magnetic anisotropy.

As a device that solves these three problems, we have proposed 3D magnetic memory using artificial ferromagnets[19]. Since the DWs of this artificial ferromagnet are confined in the DW layer, a high degree of control over the position of the DW is possible. Simulations have also confirmed that by adjusting the material parameters of the bit layer and DW layer, both high thermal stability and low DW drive current can be achieved[20]. Furthermore, by using an artificial ferromagnet consisting of a bit layer with large magnetic anisotropy and a DW layer with small magnetic anisotropy, it is possible to dramatically reduce the DW width[19]. Thus, 3D magnetic memory using artificial ferromagnets is expected to have high performance, but the problem is that the reading method is destructive. In this paper, we propose a nondestructive readout method for 3D magnetic memory and confirm its feasibility by simulations.

Corresponding author:
T. Ono (e-mail: ono@scl.kyoto-u.ac.jp).

## 2. Memory operation scheme

Figure 1(a) shows a schematic illustration of a pillar composed of bit layers and DW layers of the 3D DW motion memory. To avoid the magnetization of cells in DW layer perform as a vortex structure, the shape of the pillar is set to an ellipse[19]. When an electric current is applied to the heavy metal layer, the polarized spins flow into the bit layer directly above due to the spin Hall effect, the magnetization of the bit layer is switched, and a DW is generated in the DW layer above the bit layer. This is the bit writing process. Then, by passing a current through the pillar and DW shifting, the written bit is shifted to any bit layer in the column. By repeating this writing and shifting processes, an arbitrary sequence of information bits can be written into the column. The readout method in the previously proposed device is as follows[19]. By passing an electric current through the column and shifting the DWs, the bit information is sequentially moved upward. The moved bit information can be read as an electrical signal by the magnetic tunnel junction (MTJ) at the topmost part. This method is an efficient method that can read all bit information in the pillar at once, but it is a destructive readout method in which all bit information disappears after the readout.

Here, we propose the non-destructive readout method. Figure 1 (b) shows the bit information recorded in the pillar. Here, the upward magnetization ($+z$) of the bit layer represents bit 1, and the downward magnetization ($-z$) represents bit 0. Thus, in this figure, the bit information (010000) is recorded. To read this information, a current pulse is injected into the pillar to excite the magnetization dynamics by the spin transfer

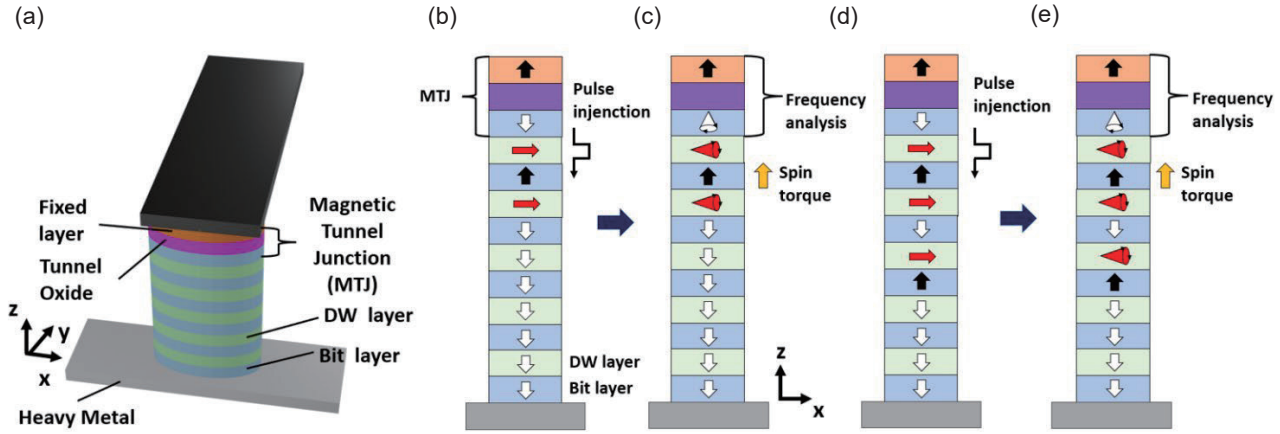


**Fig. 1** (a) Schematic illustration of a pillar composed of bit layers and DW layers of the 3D DW motion memory. (b) - (e) Operation principle of non-destructive readout method (b), (c) for bit information of (010000) and (d), (e) for bit information of (010100).

torque. The amplitude of the pulse current is set to induce sufficient magnetization oscillations due to the spin transfer torque, while ensuring that no DW shift occurs. After the pulse injection, the magnetization of each layer exhibits oscillation with different frequencies and amplitudes (Fig. 1(c)). Applying the same operation on the different bit information, such as (010100) (Fig. 1(d)), should result in the different magnetization dynamics from that for the bit information (010000). Therefore, it is feasible to determine the bit information by comparing different complex magnetization dynamics induced by the pulse current injection. While detecting the magnetization dynamics of all layers in the pillar is technically challenging, the magnetization dynamics of the topmost bit layer can be measured as a time-dependent resistance change in the MTJ. Below, we demonstrate through the simulation that it is possible to identify the bit information in the pillar by analyzing the magnetization dynamics of the topmost bit layer.

## 3. Micromagnetic analysis

Figures 2(a) and 2(b) show the bit information assumed in the following simulation, corresponding to bit information (1000) and (1011), respectively. Micromagnetic simulations were performed using mumax3.9.1, a GPU-accelerated simulation program, to verify the operation of the nondestructive readout method proposed above[21]. In the simulation, the pillar is elliptical shape with a major axis of 20 nm and a minor axis of 10 nm, and the thicknesses of the bit layer and the DW layer are 4 nm. The size of the magnetic cells is defined as a cube of 1 nm × 1 nm × 1 nm. The material parameters of the bit layer are the saturation magnetization $M_s = 8 \times 10^5$ A m$^{-1}$, the Gilbert damping constant $\alpha = 0.01$, the uniaxial magnetic anisotropy energy $K_u = 10^6$ J m$^{-3}$, and the exchange constant $A_{ex} = 10$ pJ m$^{-1}$. The material parameters of the DW layer are $M_s = 8 \times 10^5$ A m$^{-1}$, $\alpha = 0.01$, $K_u = 0$ J m$^{-3}$, and $A_{ex} = 1.2$ pJ m$^{-1}$.

Figures 2(c) and 2(d) are the time evolutions of the $z$-

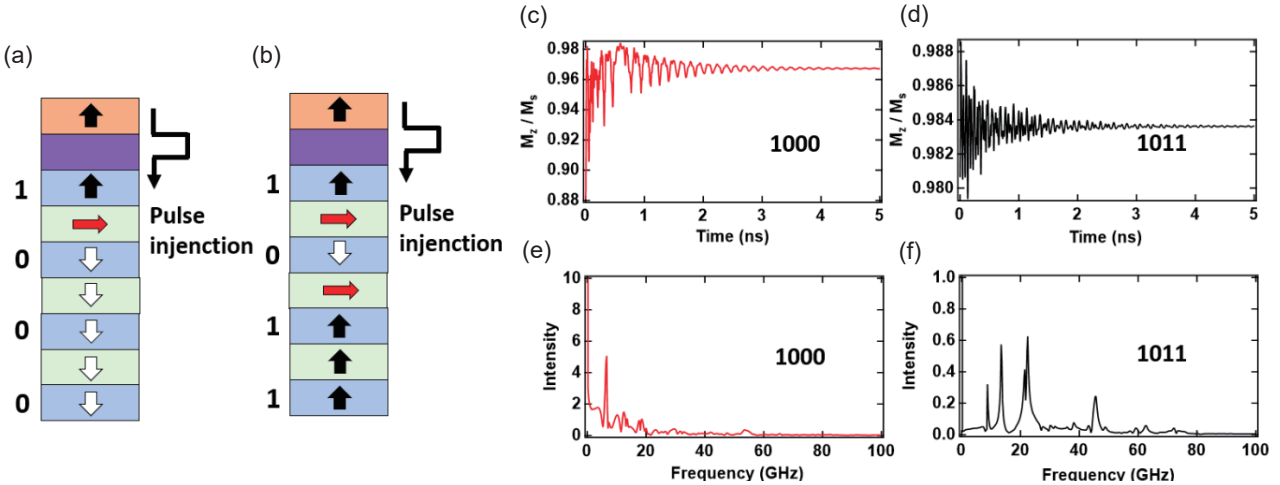


**Fig. 2**. (a), (b) Schematic illustrations of different bit informations of (1000) and (1011). (c), (d) Time evolutions of the z-component of the magnetizations ($m_z$) in the topmost bit layer after the current pulse injection. (e), (f) Results of the Fast Fourier Transforms (FFT) of the data in Figs. 2(c) and 2(d), respectively.

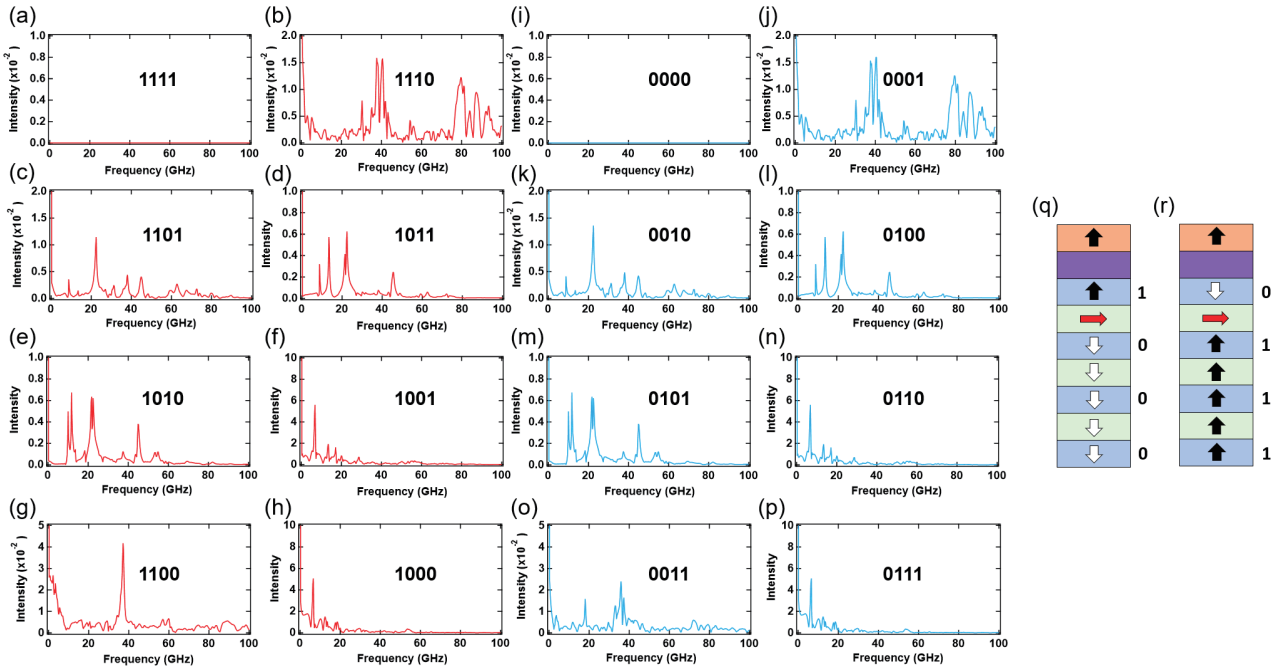


**Fig. 3** (a)-(p) FFT results of 16 possible configurations in 4-bit memory. (q) , (r) Magnetization configurations of (1000) and (0111)

component of the magnetization normalized by $M_S$ ($M_z/M_S$) in the topmost bit layer after the current pulse injection with the current density of $2\times10^{11}$ A m$^{-2}$ and the pulse length of 0.1 ns, respectively. The easy axis of magnetization in the bit layers are oriented perpendicular to the plane ($z$-axis), but due to the influence of the demagnetizing field, the magnetization around the pillar edge is slightly tilted towards the in-plane direction. As a result, oscillations in the $z$-component of the magnetization due to the spin-transfer torque are observed. Figures 2(e) and 2(f) are the results of the fast Fourier transforms (FFT) of the data in Figs. 2(c) and 2(d), respectively. The results show that it is possible to distinguish the different bit information (1000) and (1011) only by detecting the time evolution of the magnetization of the top layer.

Now we show all 16 possible results in 4-bit memory. Figure 3 shows the FFT results. As shown in Figs. 3(a)-3(h), we can easily distinguish the bit information (1111), (1110), (1101), (1011), (1010), (1001), (1100), and (1000). However, the FFT results of Figs. 3(i)-3(p) are very similar to those of Figs. 3(a)-3(h). This is because they have an anti-symmetric magnetization configuration to each other. The magnetization configurations of (1000) and (0111) are shown in Figs. 3(q) and 3(r) as an example. They should show the same magnetization dynamics. However, this degeneracy can be resolved by considering the phase of the magnetization oscillation or the offset resistance measured by the MTJ, as explained below.

Figure 4 presents the expected outputs inferred from the change in topmost magnetization from the MTJ for (1000) and (0111). The direction of the top bit layer magnetization of (1000) is parallel to the fixed layer magnetization of the MTJ, while that of (0111) is antiparallel to the fixed layer magnetization of MTJ, as shown in Figs. 3(q) and 3(r). Therefore, as shown in Fig. 4, the output for (0111) oscillates around the high resistance $R_{high}$, while that for (1000) oscillates around the low resistance $R_{low}$, leading to distinction between (1000) and (0111). Noted that, in addition to the difference in the baseline of the resistance, as shown in Fig. 4, the phase of the oscillation between (1000) and (0111) is reversed, which also distinguishes the two states.

## 4. Conclusion

We proposed the novel scheme for the non-destructive readout method in 3D magnetic DW memory and demonstrated the feasibility of the method by micromagnetic simulations. Here we have shown that 16 different identifications in 4-bit memory are possible. In principle, the proposed method can be used to read information from memory with more bits. As the number of bits increases, it is expected to become more difficult to identify bit information. In addition, it is necessary to

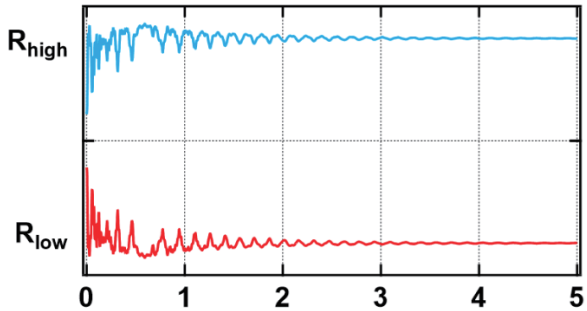


**Fig 4.** Time evolution of the tunneling magnetoresistance for the bit information of (1000) [red] and (0111) [blue].

consider the interaction with neighboring elements in actual memory. Discussion of these issues requires large-scale calculations and is a topic for future work. The readout method proposed in this paper would require a different detection circuit than conventional memories. The evaluation of device performance, including the detection circuitry, is a future issue.

**Acknowledgements** This work was partly supported by JST-CREST (JPMJCR21C1), X-NICS (JPJ011438), Cooperative Research Project Program of the Research Institute of Electrical Communication, Tohoku University, and Collaborative Research Program of the Institute for Chemical Research, Kyoto University.

## References

1) L. Berger, *J. Appl. Phys.* **71**, 2721 (1992).
2) G. Tatara, and H. Kohno, *Phys. Rev. Lett.* **92**, 086601 (2004).
3) A. Yamaguchi *et al.*, *Phys. Rev. Lett.* **92**, 077205 (2004).
4) N. Vernier, D. A. Allwood, D. Atkinson, M. D. Cooke, and R. P. Cowburn, *Europhys. Lett.* **65**, 526 (2004).
5) M. Kläui *et al.*, *Phys. Rev. Lett.* **94**, 106601 (2005).
6) M. Yamanouchi, D. Chiba, F. Matsukura, and Ohno, *Nature* **428**, 539 (2004).
7) S. Parkin, M. Hayashi, and L. Thomas, *Science*, **320**, 190 (2008).
8) T. Ono, H. Miyajima, K. Shigeto, and T. Shinjo, *Appl. Phys. Lett.*, **72**, 1116 (1998).
9) H. Tanigawa, K. Kondou, T. Koyama, K. Nakano, S. Kasai, N. Ohshima, S. Fukami, N. Ishiwata, and T. Ono, *Appl. Phys. Express,* **1**, 011301 (2008).
10) T. Koyama, G. Yamada, H. Tanigawa, S. Kasai, N. Ohshima, S. Fukami, N. Ishiwata, Y. Nakatani, and T. Ono, *Appl. Phys. Express*, **1**, 101303 (2008).
11) H. Tanigawa *et al.*, *Appl. Phys. Express.* **2**, 053002 (2009).
12) S.-W. Jung, W. Kim, T.-D. Lee, K.-J. Lee, and H.-W. Lee, *Appl. Phys. Lett.* **92**, 202508 (2008).
13) S. Fukami, *et al*, *2009 Symposium on VLSI Technology, Digest of Technical Papers*, **230**, (2009).
14) D. Chiba *et al.*, *Appl. Phys. Express,* **3**, 073004 (2010).
15) I. M. Miron *et al.*, *Nature Mater.* **10**, 419 (2011).
16) S. Emori, U. Bauer, S. M. Ahn, E. Martinez, and G. S. D. Beach, *Nature Mater.* **12**, 611–616 (2013).
17) K. S. Ryu, L. Thomas, S. H. Yang, and S. S. P. Parkin, *Nature Nanotech.* **8**, 527–533 (2013)
18) S. H. Yang, K. S. Ryu, and S. S. P. Parkin, *Nature Nanotech,* **10**, 221–226 (2014)
19) Y. M. Hung *et al.*, *J. Magn. Soc. Jpn.* **45**, 6 (2021)
20) Y. M. Hung *et al.*, *Appl. Phys. Express,* **14**, 023001 (2021)
21) A. Vansteenkiste, J. Leliaert, M. Dvornik, M. Helsen, F. G. Sanchez, and B. V. Waeyenberge, The design and verification of Mumax3, *AIP Adv.* **4**, 10713 (2014).

**Received Oct. 09, 2024; Accepted Nov. 9, 2024**

Copyright ©2024 by the Magnetics Society of Japan.
This article is licensed under the Creative Commons Attribution International License (CC BY 4.0)
http://creativecommons.org/licenses/by/4.0/



J. Magn. Soc. Jpn., **49**, 13-16 (2025) <Letter>

# Spin wave nonreciprocity due to asymmetry of propagation length

Haruka Komiyama[1], Ryusuke Hisatomi[1,2,3], Kotaro Taga[1], Hiroki Matsumoto[1], Hideki Narita[1,3], Shutaro Karube[1,2,3], Yoichi Shiota[1,2], and Teruo Ono[1,2]

[1]Institute for Chemical Research (ICR), Kyoto Univ., *Gokasho, Uji, Kyoto 611-0011, Japan*

[2]Center for Spintronics Research Network (CSRN), Kyoto Univ., *Gokasho, Uji, Kyoto 611-0011, Japan*

[3]PRESTO, Japan Science and Technology Agency, *Kawaguchi-shi, Saitama 332-0012, Japan*

Nonreciprocity of spin waves, which means the difference in amplitude depending on the direction of propagation, provides functionality to spin wave-based devices. One of the known origins of spin wave nonreciprocity is the asymmetry of the excitation efficiency due to the asymmetry of the out-of-plane microwave magnetic field generated by an antenna. We investigate the magnetic field angle dependence of spin wave nonreciprocity. We find that this nonreciprocity is due to the asymmetry of the propagation length in addition to the asymmetry of the excitation efficiency.

**Keywords:** nonreciprocity, spin wave, magneto-optical imaging, magnetic thin film, propagation length, dissipation

## 1. Introduction

Spin waves in a magnetic thin film on a substrate are expected to be next-generation information carriers because they can transmit information with low power consumption without charge transfer. Furthermore, spin waves have nonreciprocity, meaning their behavior depends on the propagation direction. Understanding the nonreciprocity of spin waves is directly linked to constructing magnonic logic circuits [1)-4)].

In a magnetic thin film thinner enough than the wavelength, a microstrip antenna's spin wave excitation efficiency depends on the propagation direction due to the asymmetry of the out-of-plane microwave magnetic field, creating the amplitude nonreciprocity. The effect is theoretically suggested to depend on the relative angle between the direction of the propagation and the magnetic field. Previous researches investigated nonreciprocity when the relative angles are 90 degrees and 0 degrees, finding that the behavior was consistent with the theoretical suggestions [5),6)].

In this study, we investigate the nonreciprocity at intermediate angles and find that it reaches a local maximum at two specific angle regions. The above mechanism cannot explain all of this angle dependence, implying that another mechanism causes the nonreciprocity. By optical imaging of the spin waves, we find that the spin wave propagation length is asymmetric. Our results suggest that the nonreciprocity of the spin waves is characterized by both the asymmetry of the excitation efficiency and the propagation length.

## 2. Experiments and Results

### 2.1 Device preparation

Figure 1(a) shows a schematic illustration of the device and the electrical transmission measurement system. We first deposit 100 μm × 100 μm-sized CoFeB (50) and Ta (2) on a thermally oxidized Si substrate using magnetron sputtering. The numbers in parentheses indicate the thicknesses of the films, and the unit is nm. After that, we deposit $SiO_2$ (60) as an insulating layer and then deposit two 0.5 μm -wide, 130 μm -long microstrip antennas for exciting and detecting spin waves. The antennas are made of Ti (5)/ Cu (150)/ Au (20) and are 10 μm apart.

### 2.2 Electrical measurements

To investigate the nonreciprocity of spin waves between the two antennas, we obtain the transmission coefficients $S_{12}$ and $S_{21}$ using a vector network analyzer (VNA) under the conditions shown in Fig. 1(a) where an in-plane magnetic field $H_{\mathrm{DC}}$ is applied in the direction of the angle $\theta$ from the $x$-axis. To avoid additional dissipation due to the nonlinearity of the spin waves, we set the microwave power input from the VNA to the antenna to −5 dBm. The frequency range for the transmission measurements is set to 3 to 20 GHz in 11.5 MHz steps, and the IF bandwidth is set to 10 kHz. The in-plane magnetic field $\mu_0 H_{\mathrm{DC}}$ is set in the range from 200 mT to 0 mT in 10 mT steps, and the magnetic field angle $\theta$ is set in the range from 0 to 90 degrees in 5 degrees steps. Here, $\mu_0$ is the vacuum permeability. The obtained transmission spectrum is usually a superposition of the electromagnetic wave signal (i.e., cross-talk) and the propagating spin wave signal. To remove the cross-talk signal, we use the spectrum at 250 mT as a reference, which contains only the cross-talk because the resonance frequencies of the spin waves excited by the antenna are outside the measurement frequency range. We obtain the spectrum of the spin waves by subtracting the reference spectrum from all the spectra at each magnetic field angle $\theta$.

Figure 1(b) shows the amplitude of the spin wave transmission spectrum measured at $\theta = 90$ degrees and $\mu_0 H_{\mathrm{DC}} = 50$ mT, for example. The gray dotted and solid lines represent the frequencies of spin waves with wavenumbers of 0 and 1 $\mu\mathrm{m}^{-1}$, respectively, calculated

Corresponding author: H. Komiyama
(e-mail: komiyama.haruka.64v@st.kyoto-u.ac.jp).

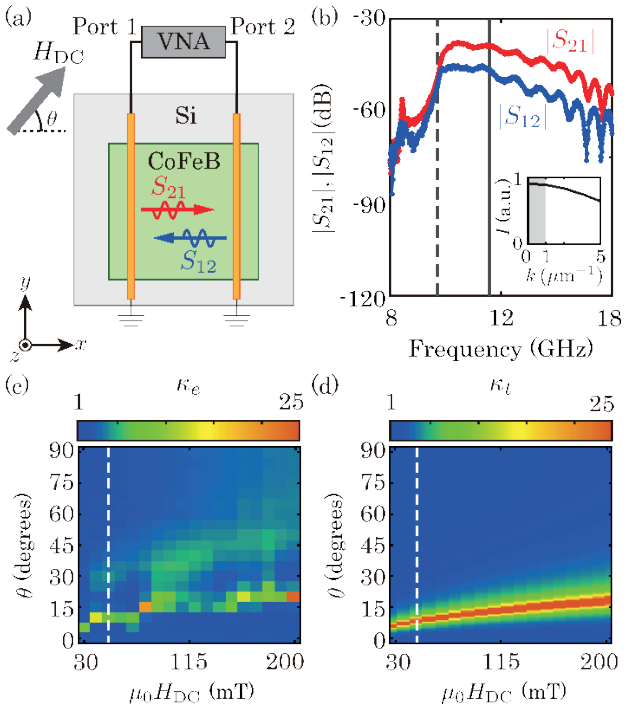


Fig. 1 (a) Experimental setup and device for observing nonreciprocity of spin waves by electrical transmission measurements. (b) Microwave transmission spectra under external magnetic field $\mu_0 H_{\mathrm{DC}} = 50$ mT and angle $\theta = 90$ degrees. Inset shows FFT intensity $I$ of antenna. (c)(d) Color maps of nonreciprocity of spin waves from (c) experiment $\kappa_e$ and (d) theoretical model $\kappa_t$.

from the known dispersion relation of the spin waves [7]. The result in Fig. 1(b) reflects the fact that the antenna of this device can efficiently excite and detect the spin waves with the wavenumbers from 0 to 1 $\mu$m$^{-1}$, as predicted from the Fourier transform of the antenna shape shown in the inset of Fig. 1(b). Furthermore, the difference in the transmission amplitudes of $|S_{21}|$ and $|S_{12}|$ represents nonreciprocity. We confirm that the transmission signal of the spin waves with the wavenumbers from 0 to 1 $\mu$m$^{-1}$ is dominant under other magnetic field conditions.

To discuss the magnetic field angle $\theta$ and magnitude $H_{\mathrm{DC}}$ dependences of the nonreciprocity, we define the nonreciprocity evaluated from the experiment as $\kappa_e(\theta, H_{\mathrm{DC}}) = \sum_{\omega_a(|k|=0)}^{\omega_a(|k|=1\,\mu\mathrm{m}^{-1})} |S_{21}| / \sum_{\omega_a(|k|=0)}^{\omega_a(|k|=1\,\mu\mathrm{m}^{-1})} |S_{12}|$. Here, we take the sum of the transmission amplitude in the frequency range of the spin waves with the wavenumbers $|k|$ of 0 to 1 $\mu$m$^{-1}$ for each $\theta$ and $H_{\mathrm{DC}}$. Figure 1(c) shows the nonreciprocity $\kappa_e$ as a function of the magnetic field magnitude $\mu_0 H_{\mathrm{DC}}$ and angle $\theta$. We omit the data below $\mu_0 H_{\mathrm{DC}} = 20$ mT, where the magnetic thin film's magnetic structure is multi-domain. Figure 1(c) shows the two-angle region where the nonreciprocity reaches the local maximum at each magnetic field magnitude: around 10 to 20 degrees and 30 to 60 degrees.

To study the origin of the nonreciprocity in the experiment, we calculate the nonreciprocity $\kappa_t$ derived from the asymmetries of spin wave excitation efficiency by the antenna depending on the propagation direction, which is demonstrated in the previous studies [5),6)], and compare it with Fig. 1(c). Based on the previous studies, the theoretical model $\kappa_t(\theta, H_{\mathrm{DC}})$ can be written as

$$\kappa_t(\theta, H_{\mathrm{DC}}) = \frac{\sum |S_{21}|}{\sum |S_{12}|} = \left( \frac{\sum_{\omega_a(|k|=0)}^{\omega_a(|k|=1\,\mu\mathrm{m}^{-1})} \omega_M \omega_a \sin\theta + \{\omega_a^2 - \omega_H^2\}}{\sum_{\omega_a(|k|=0)}^{\omega_a(|k|=1\,\mu\mathrm{m}^{-1})} \omega_M \omega_a \sin\theta - \{\omega_a^2 - \omega_H^2\}} \right), \quad (1)$$

where $\omega_M = \gamma \mu_0 M_s$ and $\omega_H = \gamma \mu_0 H_{\mathrm{DC}}$. Here, $\gamma = 2\pi \times 30$ GHz/T and $\mu_0 M_S = 1.6$ T are the gyromagnetic ratio and saturation magnetization of CoFeB, respectively. $\omega_a$ is the resonance frequency of the spin waves [7] with the wavenumber $k$ in the given $\theta$ and $H_{\mathrm{DC}}$. The first and second terms in the numerator and denominator of Eq. (1) represent the excitation efficiency of the spin waves excited by the in-plane and out-of-plane microwave magnetic fields applied from the antenna, respectively. The signs between the first and second terms, positive and negative in the numerator and denominator, respectively, represent the difference in the sum of the spin wave excitation efficiency. Note that the $\sin\theta$ in the first terms mean that the in-plane microwave magnetic field component perpendicular to the equilibrium magnetization contributes to the spin wave excitation.

Figure 1(d) is the magnetic field magnitude and angle dependences of nonreciprocity $\kappa_t$ calculated using Eq. (1). The calculation uses parameter steps of 10 mT for $\mu_0 H_{DC}$ and 0.1 degrees for $\theta$. By comparing Figs. 1(c) and 1(d), we find that the model agrees well with the local maximum of nonreciprocity in the low-angle region, around 10 to 20 degrees. However, the model does not explain the other local maximum in the high-angle region, around 30 to 60 degrees, in Fig. 1(c). The result suggests the existence of another origin of the spin wave nonreciprocity.

Generally, the amplitude of a locally excited wave at a distance $|x|$ from the excitation source can be expressed as $Ae^{-|x|/\lambda}$, where $A$ and $\lambda$ are an amplitude at the excitation source and a propagation length, respectively. Hence, the properties of the amplitude $A$ and the propagation length $\lambda$ of the waves propagating in opposite directions determine the wave nonreciprocity. For the spin waves, the existing model $\kappa_t$ in Eq. (1) only considers the asymmetry of the amplitude at the excitation source $A$. We hypothesize that the asymmetry of the propagation length is the origin of the local maximum of the nonreciprocity $\kappa_e$ in the angle region, around 30 to 60 degrees.

The above discussion can be summarized

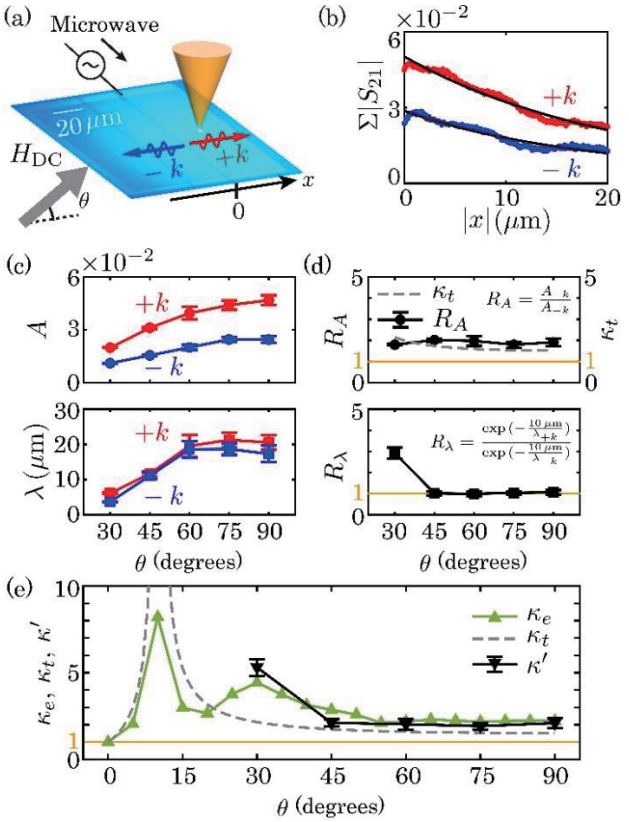


**Fig. 2** (a) Optical measurement setup including microscope image of device. (b) Distance $|x|$ dependence of sum of transmission coefficient amplitudes at $\theta = 90$ degrees, 50 mT. Solid black lines are fitting curves. (c) Angle $\theta$ dependence of amplitude $A_{\pm k}$ and propagation length $\lambda_{\pm k}$ at 50 mT. (d) Angle $\theta$ dependence of amplitude ratio $R_A$ and propagation length ratio $R_\lambda$ at $|x| = 10$ μm, using results of (c). Yellow line represents 1. (e) Angle $\theta$ dependence of nonreciprocity $\kappa_e$, $\kappa_t$, and $\kappa'$ at 50 mT.

mathematically as follows. The amplitude at the excitation source and the propagation length of the spin waves propagating in the $\pm k$ directions are represented by $A_{\pm k}$ and $\lambda_{\pm k}$, respectively. The nonreciprocity $\kappa'$ resulting from the asymmetries of the amplitude and the propagation length can be described by

$$\kappa' = \frac{A_{+k}e^{-\frac{|x|}{\lambda_{+k}}}}{A_{-k}e^{-\frac{|x|}{\lambda_{-k}}}} = \frac{A_{+k}}{A_{-k}} \times \frac{e^{-\frac{|x|}{\lambda_{+k}}}}{e^{-\frac{|x|}{\lambda_{-k}}}}. \quad (2)$$

It is expressed as the product of the ratio $R_A = A_{+k}/A_{-k}$ and the ratio $R_\lambda = e^{-|x|/\lambda_{+k}}/e^{-|x|/\lambda_{-k}}$. The $\kappa_t$ in Eq. (1) only considers the asymmetry of the excitation efficiency of the antenna and is equal to the $R_A$.

### 2.3 Magneto-Optical Kerr effect spectroscopy

To validate our above hypothesis, we investigate $R_A$, $R_\lambda$, and $\kappa'$ using optical imaging with the heterodyne-magneto-optical Kerr effect (MOKE) technique [8),9)]. Figure 2(a) shows the schematic illustration of the optical measurement setup. An in-plane external magnetic field $H_{DC}$ is applied in the direction of the angle $\theta$ from the $x$-axis. As in the electrical transmission measurements, the spin waves are excited by applying microwaves to the microstrip antenna connected to Port 1 of the VNA, and the excited spin wave propagates in the $\pm k$ directions, which correspond to the $\pm x$ directions, respectively. From the $z$-direction, a linearly polarized laser beam with a wavelength of 660 nm is input and focused on the surface of the thin magnetic film where the spin waves are excited. The optical spot diameter is about 2 μm. The polarization of the light reflected from the thin film surface, where the spin waves exist, rotates at the spin wave frequency due to the polar Kerr effect. This dynamic rotation is converted into dynamic intensity modulation by passing through a half-wave plate and a polarizing beam splitter, which is electrically detected at Port 2 of the VNA via a photodiode.

The transmission coefficient $S_{21,\pm k}$ is obtained at each optical spot position $x$ for the spin waves in the $\pm k$ directions. The antenna position is $x = 0$, as shown in Fig. 2(a). The output power from the VNA is set to −5 dBm, the frequency range is 8.5 to 18 GHz in 11.5 MHz steps, and the IF bandwidth is set to 100 Hz. We use the device shown in Fig. 2(a) for optical imaging measurements, which has a different antenna separation distance of 25 μm from the device for the electrical transmission measurements shown in Fig. 1(a). All other designs are the same. The reason for increasing the antenna separation distance is to suppress the effect of the spin waves propagating in the $-k$ direction being reflected by the other antenna.

Figure 2(b) shows the distance $|x|$ dependence of the sum of the transmission coefficient amplitude $\sum_{\omega_a(|k|=0)}^{\omega_a(|k|=1\ \mu m^{-1})} |S_{21,\pm k}|$ under $\theta = 90$ degrees and $\mu_0 H_{DC} = 50$ mT. The black lines show the fitting results using $A_{\pm k}e^{-x/\lambda_{\pm k}}$. The red and blue plots in the upper and lower panels of Fig. 2(c) show the magnetic field angle dependence of the fitting parameters: the amplitude $A_{\pm k}$ and propagation length $\lambda_{\pm k}$. Note that the results for angles of less than 30 degrees are not obtained because preliminary experiments confirm that the spin wave excitation efficiency is low and the signal-to-noise ratio of the optical measurement is low. Figure 2(d) shows the angular dependence of the ratio $R_A = A_{+k}/A_{-k}$ and $R_\lambda = \exp\left(-\frac{10\ \mu m}{\lambda_{+k}}\right)/\exp\left(-\frac{10\ \mu m}{\lambda_{-k}}\right)$, obtained from the amplitude and propagation length obtained by the fitting. We use $|x| = 10$ μm for $R_\lambda$ calculation to study spin wave propagation in the device with a 10 μm distance between the antennas, which is used in the electrical measurement. The upper panel of Fig. 2(d) shows that $R_A$ and the theoretical value $\kappa_t$ agree quantitatively. From the lower panel, $R_\lambda$ is not always 1, increasing at $\theta = 30$ degrees. These results indicate that the propagation length is not symmetrical. As Fig.

2(e) shows, the angular dependence of the nonreciprocity $\kappa_e$ from the electrical measurement is not reproduced by the theoretical value $\kappa_t$, represented as white lines in Figs. 1(c) and 1(d), respectively. However, the angular dependence of $\kappa' = R_A \times R_\lambda$, including the propagation length asymmetry, is consistent with that of $\kappa_e$ above 30 degrees . The results demonstrate that the nonreciprocity $\kappa_e$ around 30 degrees is due to the asymmetry of the propagation length. For the origin of the nonreciprocity, it is essential to consider the contributions of both the asymmetries of the excitation efficiency and the propagation length.

Possible mechanisms of the asymmetry of the spin wave propagation length are the following: the asymmetry of the dissipation of the spin wave energy to other physical systems due to the spin pumping [10),11)] or the phonon-magnon coupling [12)-14)] and the asymmetry of the dispersion relation due to the Dzyaloshinskii-Moriya interaction (DMI) [15),16)]. Further investigation is required to discuss the relationship between our results and these effects.

Comparing $\kappa'$ and $\kappa_e$ at magnetic field angles of less than 30 degrees is important for discussing the origin of the observed nonreciprocity in more detail. For this purpose, the future outlook is to improve the signal-to-noise ratio of optical measurements by making spin wave excitation antennas more efficient and enhancing optical signals.

## 3. Conclusion

In this study, we investigate the angular dependence of the nonreciprocity of the spin wave in the magnetic thin film using electrical transmission measurements. We find that the existence of nonreciprocity that cannot be explained by the previously known asymmetry of the spin wave excitation efficiency. By performing optical imaging, we confirm that the nonreciprocity is due to the direction-dependent spin wave propagation length. Results obtained in this study will be helpful for future research on information transport devices using spin waves.

**Acknowledgements** This work was supported by JSPS KAKENHI (grant no. JP21K18145, JP22K14589, JP22KJ1995, JP23KJ1209, JP23KJ1159, JP24H00007, JP24H02233), JST (grant no. JPMJFS2123, JPMJPR200A), MEXT Initiative to Establish Next-generation Novel Integrated Circuits Centers (X-NICS) (grant no. JPJ011438), and the Collaborative Research Program of the Institute for Chemical Research, Kyoto University.

## References

1) K. Sekiguchi, K. Yamada, S. M. Seo, K.-J. Lee, D. Chiba, K. Kobayashi, and T. Ono: *Appl. Phys. Lett.*, **97**, 022508 (2010).
2) M. Jamali, J. H. Kwon, S. M. Seo, K. J. Lee, and H. Yang: *Sci. Rep.*, **3**, 3160 (2013).
3) J. Chen, H. Yu, and G. Gubbiotti: *J. Phys. D Appl. Phys.*, **55**, 123001 (2022).
4) B. Flebus, D. Grundler, B. Rana, Y. Otani, I. Barsukov, A. Barman, G. Gubbiotti, P. Landeros, J. Akerman, U. S. Ebels, P. Pirro, V. E. Demidov, K. Schultheiss, G. Csaba, Q. Wang, D. E. Nikonov, F. Ciubotaru, P. Che, R. hertel, T. Ono, D. Afanasiev, J. H. Mentink, T. Rasing, B. Hillebrands, S. Viola Kusminskiy, W. Zhang, C. R. Du, A. Finco, T. van der Sar, Y. K. Luo, Y. Shiota, J. Sklenar, T. Yu, and J. Rao: *J. Phys.: Condens. Matter*, **36**, 363501 (2024).
5) T. Schneider, A. A. Serga, T. Neumann, B. Hillebrands, and M. P. Kostylev, *Phys. Rev. B*, **77**, 214411 (2008).
6) M. Nakayama, K. Yamanoi, S. Kasai, S. Mitani, and T. Manago: *Jpn. J. Appl. Phys.*, **54**, 083002 (2015).
7) B. A. Kalinikos and A. N. Slavin: *J. Phys. C: Solid State Phys.*, **19**, 7013 (1986).
8) Y. Shiota, S. Funada, R. Hisatomi, T. Moriyama, and T. Ono: *Appl. Phys. Lett.*, **116**, 192411 (2020).
9) Y. Shiota, R. Hisatomi, T. Moriyama, and T. Ono: *Phys. Rev. B*, **102**, 214440 (2020).
10) S. Mizukami, Y. Ando, and T. Miyazaki: *Phys. Rev. B*, **66**, 104413 (2002).
11) J. H. Kwon, J. Yoon, P. Deorani, J. M. Lee, J. Sinha, K. -J. Lee, M. Hayashi, and H. Yang: *Sci. Adv.*, **2**, e1501892 (2016).
12) R. Sasaki, Y. Nii, Y. Iguchi, and Y. Onose: *Phys. Rev. B*, **95**, 020407 (2017).
13) S. Streib, H. Keshtgar, and G. E. W. Bauer: *Phys. Rev. Lett.*, **121**, 027202 (2018).
14) R. Schlitz, L. Siegl, T. Sato, W. Yu, G. E. W. Bauer, H. Huebl, and S. T. B. Goennenwein: *Phys. Rev. B*, **106**, 014407 (2022).
15) F. Garcia-Sanchez, P. Borys, A. Vansteenkiste, J. Kim, and R. L. Stamps: *Phys. Rev. B*, **89**, 224408 (2014).
16) M. Kuepferling, A. Casiraghi, G. Soares, G. Durin, F. Garcia-Sanchez, L. Chen, C. H. Back, C. H. Marrows, S. Tacchi, and G. Carlotti: *Rev. Mod. Phys.*, **95**, 015003 (2023).

**Received Oct. 23, 2024; Accepted Nov. 15, 2024**

Copyright ©2024 by the Magnetics Society of Japan.
This article is licensed under the Creative Commons Attribution International License (CC BY 4.0)
http://creativecommons.org/licenses/by/4.0/



J. Magn. Soc. Jpn., **49**, 17-20 (2025) <Letter>

# Generation of phonons with out-of-plane angular momentum by superposition of longitudinal surface acoustic phonons

Kotaro Taga*, Ryusuke Hisatomi*,**,***, Ryo Sasaki***,****, Haruka Komiyama*, Hiroki Matsumoto*, Hideki Narita*,***, Shutaro Karube*,**,***, Yoichi Shiota*,**, and Teruo Ono*,**

* Institute for Chemical Research (ICR), Kyoto Univ., *Gokasho, Uji, Kyoto 611-0011, Japan*
** Center for Spintronics Research Network (CSRN), Kyoto Univ., *Gokasho, Uji, Kyoto 611-0011, Japan*
*** PRESTO, Japan Science and Technology Agency, *Kawaguchi, Saitama 332-0012, Japan*
**** RIKEN Center for Quantum Computing (RQC), RIKEN, *Wako, Saitama 351-0198, Japan*

Circularly polarized phonons carry angular momentum, and surface acoustic waves (SAWs) offer an ideal platform for manipulating the electron spins in magnetic thin films. However, achieving phonons with out-of-plane angular momentum using easily controllable SAWs has been challenging. In this study, we demonstrate a device that superposes two longitudinal leaky SAWs (LL-SAWs) to generate spatially distributed out-of-plane angular momentum in surface acoustic phonons. By using an optical imaging setup, we measure the surface tilt associated with LL-SAWs and confirm the interference pattern resulting from their superposition. This approach to generating phonon angular momentum through superposition enables the creation of spatially distributed phonon angular momentum with easily switchable polarization, opening new avenues for phonon-based applications in spintronics.

**Keywords:** phonon angular momentum, phonon device, surface acoustic wave, optical imaging, superposition

## 1. Introduction

Phonons possess two types of angular momentum: one arises from the rotation of lattice points, and the other from the vortex of the displacement field. Recent experimental studies have demonstrated that these angular momenta can be transferred to electron spins in thin films on substrate surfaces. These couplings are a current focus in spintronics and phononics[1-4].

Rayleigh-type surface acoustic waves (SAWs), which are commonly used in the previous studies, are typical phonon modes accompanied by the two types of angular momentum. The angular momentum direction of Rayleigh-type SAWs is perpendicular to both their wave vector and in the surface plane, resulting in the angular momenta with only in-plane components.

To advance the understanding of angular momentum transfer between phonons and electron spins, we aim to develop a new type of phonon device where the phonon angular momentum is perpendicular to the surface. This out-of-plane angular momentum can align electron spins in previously unattainable directions. As illustrated in Fig. 1(a), we superimpose two orthogonally propagating pseudo-longitudinal SAWs, known as longitudinal leaky SAWs (LL-SAWs)[5,6], to realize a phonon system where the lattice points move in a perfect circle within the surface. In the region where the two LL-SAWs overlap, the lattice rotation alternates in opposite directions with respect to the $x$-axis, and the $z$ component of angular momentum $\boldsymbol{L} = \boldsymbol{u} \times \dot{\boldsymbol{u}}$ calculated from the displacement vector $\boldsymbol{u}$ exhibits a stripe-shaped distribution of positive and negative values, as shown in Fig. 1(b).

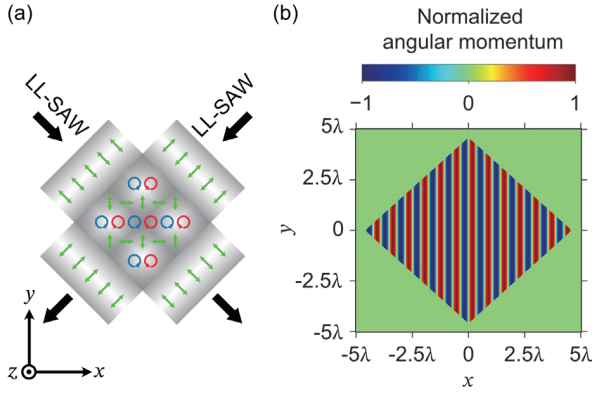


**Fig. 1** (a) Conceptual schematic of rotational motion of lattice in superposition section of orthogonally propagating longitudinal leaky SAWs (LL-SAWs). (b) Spatial distribution of $z$ component of angular momentum $\boldsymbol{L}$ originating from lattice rotation.

In this letter, we first investigate the feasibility of orthogonal propagation of LL-SAWs using COMSOL simulations. Based on the simulation results, we fabricate a device and evaluate it with electrical measurements. Finally, we visualize the SAW mode using optical imaging. The results confirm that the device functions as expected.

## 2. Simulation

We perform finite element method simulations using COMSOL to clarify the existence of longitudinal surface acoustic phonons that can be excited by an interdigital transducer (IDT) and propagate orthogonally to each other. These phonons are necessary to generate circular motion of lattice points in the plane. We select a 36°-Y cut $LiTaO_3$ single crystal, a piezoelectric crystal commonly used in phonon research[5,7]. The crystal structure on the cut surface of this substrate has symmetry about the crystal's $X$-axis, and this symmetry governs the phonon characteristics. Focusing on the symmetry of axes

Corresponding author:
K. Taga (e-mail: taga.kotaro.62d@st.kyoto-u.ac.jp).

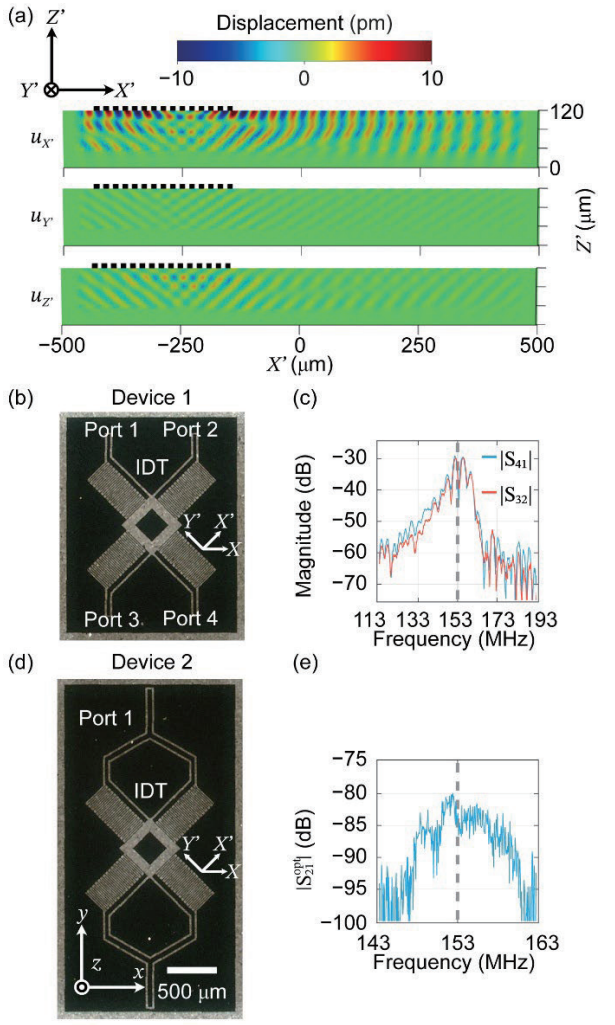


**Fig. 2** (a) COMSOL simulation result. (b) Microscope image of Device 1. (c) Rf transmission spectra of Device 1. (d) Microscope image of Device 2. (e) Spectrum of optical path modulation magnitude.

inclined at ±45° and ±135° relative to the $X$-axis, we discovered that LL-SAWs can be effectively excited in these orientations.

Figure 2(a) presents the simulation results. We define the axis inclined by 45° from the $X$-axis as the $X'$-axis. The in-plane and out-of-plane directions orthogonal to $X'$-axis are designated as $Y'$- and $Z'$-axis, respectively. An IDT designed to excite a SAW with a wavelength of 40 μm is placed on the left side of the device. The plot illustrates the displacement amplitude in each axis direction when a radio frequency (rf) voltage of 153 MHz at 0 dBm power is applied to the IDT.

The result reveals that the displacement amplitude in the $X'$-direction, indicating the longitudinal component, is predominant. This confirms the presence of a pseudo-longitudinal surface acoustic phonon. The second largest displacement observed in the $Z'$-direction enables the detection of this phonon using optical imaging techniques[8], as this component creates surface waving. Since this mode propagates from the IDT and penetrates the bulk, it is referred to as a longitudinal leaky surface acoustic wave (LL-SAW).

## 3. Experiment

### 3.1 Device fabrication and characterization

Based on the results of the COMSOL simulation, we fabricate two types of devices. Figures 2(b) and 2(d) show microscope images of these SAW devices. These SAW devices consist of four IDTs formed with Ti (5 nm) and Au (80 nm) films on a 36°-$Y$ cut $LiTaO_3$ substrate and a single pad made of the same films for optical imaging. Both devices are symmetrically arranged relative to the crystal's $X$-axis. The opposing IDT pair is designed to efficiently excite and detect SAWs with a wavelength of 40 μm. The comb width and line spacing are both 10 μm, and the number of combs is 15 pairs for all IDTs in both devices. Device 1, shown in Fig. 2(b), is used for the electrical evaluation of LL-SAWs, with each IDT's signal lines electrically isolated. In Device 2, depicted in Fig. 2(d), the signal lines of two IDTs are shorted to simultaneously excite orthogonally propagating LL-SAWs at the same power, allowing for optical evaluation of their intersection. In both devices, the central pad region is where the two waves overlap.

First, we electrically characterize the propagating SAWs in Device 1, shown in Fig. 2(b). Figure 2(c) displays the rf transmission spectrum $|S_{41}|$ ($|S_{32}|$) from Port 1 (2) to Port 4 (3) using a vector network analyzer (VNA). The broad peak around 153 MHz indicates that LL-SAWs with a wavelength of 40 μm and a frequency of 153 MHz are propagating, aligning with the COMSOL simulation results. The matching of spectra $|S_{41}|$ and $|S_{32}|$ confirms that the SAW modes of Device 1 are mirror-symmetric to the crystal's $X$-axis.

### 3.2 Optical measurement

We then employ an optical imaging method[9,10] to diagnose the superposition state of the two LL-SAWs. In Device 2, light incident perpendicularly is reflected from the surface of the device. By considering the surface as a dynamically tilting mirror, the path of the reflected light is modulated by the slight surface tilt due to the vertical surface displacement $u_Z$ shown in Fig. 2(a). Observing this optical path modulation with spatial resolution enables the visualization of the superposition of the LL-SAW modes.

The optical setup is almost identical to that in the reference[10], except that the light is incident perpendicularly and the axis for measuring optical path modulation is aligned with the $x$-axis shown in Fig. 2(d). In this setup, we use a VNA to excite LL-SAWs propagating orthogonally by applying an rf voltage of 153 MHz with a power of 10 dBm to Port 1 shown in Fig. 2(d).

The optical path modulation induced by the surface tilt $du_z/dx$ is converted into optical intensity modulation, which the photodetector then converts into an electrical signal. This signal coherently captures the dynamical surface tilt $du_z/dx$ and is fed back into Port 2 of the VNA

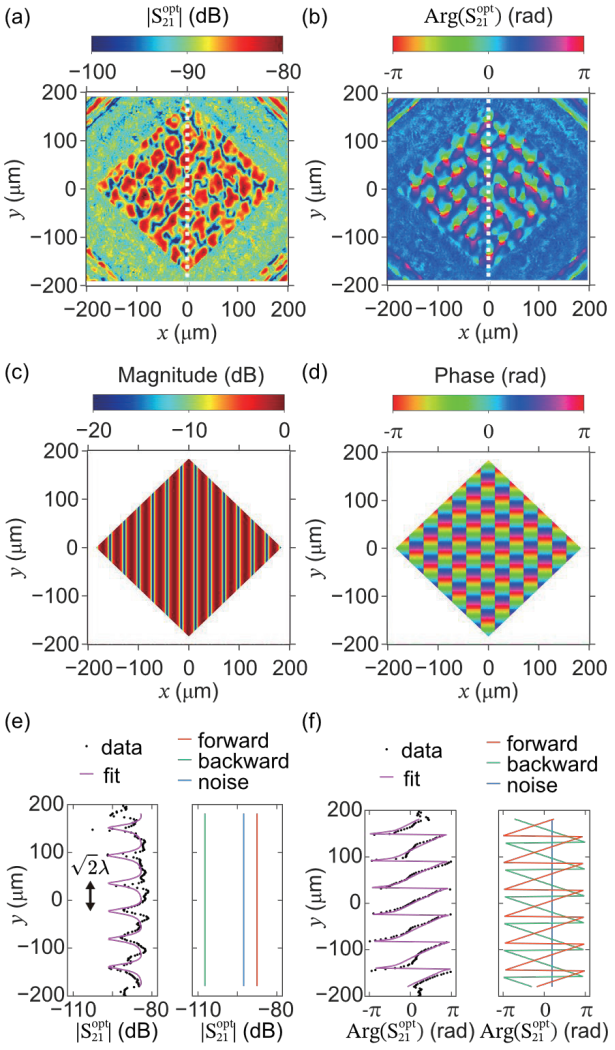


**Fig. 3** (a) Two-dimensional (2D) image of magnitude of spatially resolved optical path modulation signal. (b) 2D image of phase of spatially resolved optical path modulation signal. Phase is wrapped. (c) Calculated distribution of normalized magnitude of optical path modulation signal. (d) Calculated distribution of phase of optical path modulation signal. (e) Cross section of magnitude at $x = 0$, indicated by white dotted line in (a). In left panel, experimental data (black dots) is shown with corresponding fitting (magenta line). Right panel shows magnitude of each contribution, from forward wave (red), backward wave (green) and coherent noise (blue), extracted from fitting. (f) Cross section of phase at $x = 0$, indicated by white dotted line in (b). Layout is identical to (e).

to obtain magnitude and phase information. Since the optical spot size of 5 μm is small compared to the SAW wavelength of 40 μm, it is possible to observe the magnitude and phase of the local surface tilt $\mathrm{d}u_z/\mathrm{d}x$.

Figure 2(e) shows the magnitude spectrum of the optical path modulation when the optical spot is centered on the single metal pad shown in Fig. 2(d). The $|S_{21}^{opt}|$ spectrum reveals a magnitude peak of around 153 MHz, matching the rf transmission spectra in Fig. 2(c). This correspondence indicates that the rf signal is converted into an optical path modulation signal via the LL-SAWs.

By scanning the optical spot position on the surface, we obtain the spatial distributions of the magnitude and phase of the surface tilt $\mathrm{d}u_z/\mathrm{d}x$ associated with the LL-SAWs in Device 2. We perform a two-dimensional (2D) imaging of the optical path modulation signal around the single metal pad. Figures 3(a) and 3(b) show the magnitude and phase of the optical path modulation signal, respectively, measured by scanning the spot position of every 2 μm in both the $x$ and $y$ directions. First, we compare these mappings with theoretical calculations. Assuming here that the displacement $u_Z$ propagates in the form of a plane wave, displacement $u_Z$ at the position of $\boldsymbol{r} = (x, y)^T$, caused by a SAW propagating with a wave vector $\boldsymbol{k}(\theta) = (k_0 \cos\theta, k_0 \sin\theta)^T$, can be expressed by the equation

$$u_z(\boldsymbol{r}, t, \theta, \phi) = u_0 e^{i(\boldsymbol{k}(\theta)\cdot\boldsymbol{r} - \omega t + \phi)}, \quad (1)$$

where $u_0$ is the displacement amplitude and $\phi$ is the initial phase. Then the optical path modulation signal can be represented in its complex form as

$$\alpha(\boldsymbol{r}, t, \theta, \phi) = \alpha(\boldsymbol{r}, \theta, \phi) e^{-i\omega t}, \quad (2)$$

using the proportional relation $\alpha(\boldsymbol{r}, t, \theta, \phi) \propto \partial u_z(\boldsymbol{r}, t, \theta, \phi)/\partial x$. Considering the superposition of SAWs with $\theta_1 = -45°$ and $\theta_2 = -135°$ the calculated optical path modulation induced by the dynamical surface tilt $\partial u_z/\partial x$ is given by

$$\alpha_{\mathrm{forward}}(\boldsymbol{r}) = \alpha(\boldsymbol{r}, \theta_1, \phi_1) + \alpha(\boldsymbol{r}, \theta_2, \phi_2). \quad (3)$$

We can model $S_{21}$ parameter of the optical measurement from this complex signal. Figures 3(c) and 3(d) show the normalized magnitude and phase calculated from Eq. (3). A notable feature here is that the magnitude represents a stripe pattern, while the phase represents a lattice pattern. Comparing the experimental and calculated mappings reveals that both exhibit a lattice pattern in the phase, indicating successful superposition of orthogonally propagating LL-SAWs. However, the magnitude unexpectedly forms a lattice pattern instead of the anticipated stripe pattern predicted by the calculation. This discrepancy suggests that the result cannot be explained solely by the superposition of traveling waves.

To understand the discrepancy between experimental and calculated mappings, we examine the cross section of the 2D maps at $x = 0$, represented by the black dots in the left panels of Figures 3(e) and 3(f). The key to understanding the behavior of the magnitude is the oscillation period $\sqrt{2}\lambda \sim 56$ μm observed in the cross section. The magnitude oscillation can arise from two types of interference. The first involves interference between the forward wave signal and the backward wave reflected by the opposing IDT expressed as

$$\alpha_{\mathrm{backward}}(\boldsymbol{r}) = R_{\mathrm{ref}}[\alpha(\boldsymbol{r}, \theta_3, \phi_3) + \alpha(\boldsymbol{r}, \theta_4, \phi_4)], \quad (4)$$

where $\theta_3 = 135°$, $\theta_4 = 45°$ and $R_{\mathrm{ref}}$ is a reflectivity constant, respectively. This interference creates a standing component of the SAW with an oscillating period of $\sqrt{2}\lambda/2 \sim 28$ μm. The mismatch between the oscillation period in the experimental result and the calculated one from the standing wave indicates that this interference alone cannot explain the observed oscillation

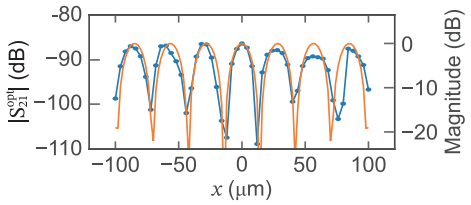


**Fig. 4** Oscillation of magnitude of optical path modulation signal in $x$-direction due to superposition of LL-SAWs. Blue dots and line represent fitted magnitude $|S_{21}^{opt}|$. Orange line represents calculated magnitude.

period.

Next, we consider the coherent noise introduced by crosstalk of the rf signal, which has a phase independent of position written as

$$\alpha_{noise} = \alpha_n e^{i\phi_n}. \quad (5)$$

The interference between the forward wave signal and this fixed-phase coherent noise results in an oscillating magnitude with a period of $\sqrt{2}\lambda \sim 56$ μm, as observed in the experiment. We model the $S_{21}^{opt}$ signal from the sum of these three contributions and fit to the experimental data, represented by the magenta line in the left panels of Figs. 3(e) and 3(f). From this fitting, the magnitude and phase of the contributions from the forward wave (red), the reflected wave (green), and the coherent noise (blue) can each be determined, as shown in the right panels of Figs. 3(e) and 3(f). The magnitude ratio clearly demonstrates that the experimental data predominantly reflects the interference between the forward wave and the coherent noise.

To further reproduce the oscillations of the calculated magnitude in $x$-direction, as seen in Fig. 3(c), the same fitting procedure is performed on the one-dimensional magnitude data from $y = -60$ μm to $y = 60$ μm, while varying the cross section line from $x = -100$ μm to $x = -100$ μm. Figure 4 shows the dependence of fitted magnitude $|S_{21}^{opt}|$ from the forward wave on the position $x$. The experimental data indicated by blue dots and line closely align with the calculated orange line. The agreement between experimental and calculated distribution of magnitude of the signal confirms the superposition of two orthogonally excited LL-SAWs.

The coherent noise observed in the experimental results is attributed to the rf signal entering from Port 1 to Port 2 of the VNA independently of the optical modulation, due to direct electromagnetic coupling. To eliminate this effect experimentally, it is necessary either to enhance the surface tilt induced by the SAW to a level where the coherent noise becomes negligible, or to optimize the wiring configuration. Utilizing a time-gating technique to remove the direct coupled electromagnetic signal could also be an effective method.

Additionally, from the fitted wavelength $\lambda = 41.2 \pm 0.1$ μm, the phase velocity is calculated to be ~ 6300 m/s, which is indicative of the high-speed characteristic of longitudinal waves. In comparison, the phase velocity of the shear horizontal mode excited in the $X$-axis direction on the same 36°-$Y$ cut substrate, is ~ 4200 m/s[7]. The high phase velocity of LL-SAW can contribute to achieving higher frequencies, including those in the GHz range, enabling operation at the typical frequencies of ferromagnetic resonance.

## 4. Conclusion

We propose a method to generate the angular momentum of phonon $\boldsymbol{L}$ in out-of-plane direction using the superposition of LL-SAWs. The COMSOL simulations reveal that LL-SAW modes on the device can be evaluated by measuring surface tilt arising from small out-of-plane displacement. By using optical path modulation imaging, we visualize this out-of-plane displacement induced by the superposition of LL-SAWs. The results confirm that longitudinal displacement is also superposed, resulting in the generation of out-of-plane angular momentum.

**Acknowledgements** This work was supported by JSPS KAKENHI Grant Number JP22KJ1995, JST PRESTO Grant Number JPMJPR200A, MEXT Initiative to Establish Next-generation Novel Integrated Circuits Centers (X-NICS) Grant Number JPJ011438, and Collaborative Research Program of the Institute for Chemical Research, Kyoto University.

## References

1) R. Sasaki, Y. Nii, and Y. Onose: *Nat. Commun.*, **12**, 2599 (2021).
2) M. Matsuo, J. Ieda, K. Harii, E. Saitoh, and S. Maekawa: *Phys. Rev. B.*, **87**, 180402 (2013).
3) D. Kobayashi, T. Yoshikawa, M. Matsuo, R. Iguchi, S. Maekawa, E. Saitoh, and Y. Nozaki: *Phys. Rev. Lett.*, **119**, 077202 (2017).
4) Y. Kurimune, M. Matsuo, and Y. Nozaki: *Phys. Rev. Lett.*, **124**, 217205 (2020).
5) S. Tonami, A. Nishikata, and Y. Shimizu: *Jpn. J. Appl. Phys.*, **34**, 2664 (1995).
6) Y. Kobayashi, N. Tanaka, Y. Baba, H. Okano, T. Usuki, K. Shibata, and Y. Shimizu: *Jpn. J. Appl. Phys.*, **36**, 6083 (1997).
7) K. Hashimoto, M. Yamaguchi, S. Mineyoshi, O. Kawachi, M. Ueda, and G. Endoh: *IEEE Ultrasonics Symp. Proc.*, **1**, 245 (1997).
8) O. Holmgren, J. V. Knuuttila, T. Makkonen, K. Kokkonen, V. P. Plessky, W. Steichen, M. Solal, and M. M. Salomaa: *Appl. Phys. Lett.*, **86**, 024101 (2005).
9) K. Taga, R. Hisatomi, Y. Ohnuma, R. Sasaki, T. Ono, Y. Nakamura, and K. Usami: *Appl. Phys. Lett.*, **119**, 181106 (2021).
10) R. Hisatomi, K. Taga, R. Sasaki, Y. Shiota, T. Moriyama, and T. Ono: *Phys. Rev. B.*, **107**, 165416 (2023).

**Received Oct. 17, 2024; Accepted Nov. 19, 2024**

Copyright ©2024 by the Magnetics Society of Japan.
This article is licensed under the Creative Commons Attribution International License (CC BY 4.0)
http://creativecommons.org/licenses/by/4.0/



J. Magn. Soc. Jpn., **49**, 21-26 (2025) <Paper>

# Feature analysis on iron loss behaviors of various soft magnetic cores under DC bias fields

T. Onuma *, N. Ono *, S. Okamoto *, **, ***

* Institute of Multidisciplinary Research for Advanced Materials (IMRAM), Tohoku University, 2-1-1 Katahira, Aoba-Ku, Sendai 980-8577, Japan

** Center for Science and Innovation in Spintronics (CSIS), Tohoku University, 2-1-1 Katahira, Aoba-Ku, Sendai 980-8577, Japan

*** National Institute for Materials Science (NIMS), Tsukuba, 305-0047, Japan

To realize a highly efficient power converter, it is very important to reduce the energy loss of passive magnetic components such as transformers and inductors in the high frequency region. Core loss behavior under DC bias magnetic fields is crucial for characterizing inductor performance. Various core loss behaviors have been reported so far, that is, the iron loss of some cores decreases with the DC bias fields while that of the others increases. These various core loss behaviors under DC bias fields have not been fully elucidated. In this study, the parameters for core loss behaviors under DC bias fields were investigated through the feature extraction of *B*-*H* curves of various soft magnetic cores with different materials and different permeabilities. Principal component analysis revealed that the slope and curvature of *B*-*H* curves are major components that are strongly correlated with core loss. Changes in the slope and curvature were found to positively and negatively contribute to core loss, respectively. Therefore, the various core loss behaviors under DC bias fields are understood to be a consequence of these two competitive factors.

**Keywords:** soft magnetic core, iron loss, DC bias, permeability, principal component analysis

## 1. Introduction

In recent years, the remarkable growth of renewable energy and electric vehicles has evoked strong demands for the downsizing and high-efficiency of power converter systems [1)-6)]. These demands are driving the development of next-generation power semiconductor devices, leading to an increase in the switching frequency of power converter systems. Consequently, losses in soft magnetic passive devices, such as transformers and inductors, have become a major contributor to the total loss of modern power converter systems, and their reduction has become a critical issue [7)-12)]. In power converter systems, such as chopper circuits, a ripple current is applied to inductors along with a DC current, corresponding to a minor *B*-*H* curve operation under a DC bias field. The core loss behavior under a DC bias field is crucially important for characterizing the performance of inductors [13)-21)]. However, various core loss behaviors with DC bias field have been reported for cores made of different magnetic materials [22)-26)]. For example, the core loss of Sendust tends to decrease with increasing DC bias field, while that of ferrite tends to increase with increasing DC bias field [22)]. These different core loss behaviors under DC bias fields have significant impacts on the design of power converter systems. While they have been attributed to the material nature, the physical mechanism has not been discussed.

Since core loss behavior under DC biased fields is a consequence of the magnetization dynamics of the soft magnetic core, the magnetization dynamics are reflected in the shape of the *B*-*H* curve under DC biased fields. The *B*-*H* curve shape was reported to change from a symmetric lenticular to a convex crescent with increasing the DC bias field [13), 20), 31)]. Therefore, the analysis of *B*-*H* curve shape under DC bias fields would be a good measure to understand the various core loss behaviors of soft magnetic cores. However, there is no adequate method to characterize the *B*-*H* curve shape. For this issue, principal component analysis (PCA), which is one of the machine learning techniques [27)-30)], was applied to characterize the *B*-*H* curve shape of Sendust powder core in our previous work [31)]. As a result, PCA extracted the features of *B*-*H* curve shape, and these features exhibited the clear relationship with the core loss of Sendust powder core with DC bias field. In this study, this approach has been applied to the soft

**Table 1** Soft magnetic cores of different magnetic materials

| Material | Fe-Si-Al (Sendust) | Fe-Si | Fe-Ni-Mo (Mo-Permalloy) | MnZn ferrite |
|---|---|---|---|---|
| Saturation magnetization $\mu_0 M_s$ (T) | 1.0 | 1.8 | 0.75 | 0.5 |
| Relative initial permeability $\mu_i$ | 60 | | | 2,900 |
| Outer diameter, inner diameter, height (mm) | 42.9, 24.2, 16.3 | | 12.7, 7.6, 4.8 | 13.0, 8.0, 5.0 |

**Table 2** Soft magnetic cores of same magnetic material with different $\mu_i$

| Material | Fe-Ni-Mo (Mo-Permalloy) | | | | |
|---|---|---|---|---|---|
| Saturation magnetization $\mu_0 M_s$ (T) | 0.75 | | | | |
| Relative initial permeability $\mu_i$ | 26 | 60 | 125 | 300 | 550 |
| Outer diameter, inner diameter, height (mm) | 12.7, 7.6, 4.8 | | | | |

Corresponding author: T. Onuma
(e-mail: tomoyuki.onuma.d7@tohoku.ac.jp).

magnetic cores of different materials and permeabilities, which exhibit various core loss behaviors under DC bias fields. We successfully demonstrated that the two major components of $B$-$H$ curve shape, which correspond the slope and curvature, exhibit a positive and negative contributions to the core loss, respectively. Consequently, the various core loss behaviors with DC bias field are understood by the contributions of these two competitive components. This paper consists of three parts. After the introduction and experiments, the core loss behaviors of various soft magnetic cores with different materials are studied. Then the core loss behaviors of same material with different permeabilities are discussed. Finally, the contributions of $B$-$H$ curve shape components to the core loss are discussed.

## 2. Experimental

Core loss measurements under DC bias fields were performed by means of a two-coil method with $B$-$H$ analyzer (IWATSU SY-8218) at a fixed peak-to-peak amplitude of magnetic flux density $\Delta B$ of 40 mT, a fixed frequency $f$ of 100 kHz, and a varying DC bias field up to 4 kA/m. A power amplifier (IWATSU SY-5002) was employed to excite the primary coil. A DC bias field was applied using a tertiary coil of coated copper wire with 0.8 mm in diameter. To protect the DC power source from the crosstalk of AC signals, choke coils (Murata 1410478C) were inserted in series of 10 between the tertiary coil and the DC power source, which was designed to be the total inductance as 100 times larger than that of tertiary winding. The number of turns of tertiary winding was adjusted in the range of 12 to 25 turns depending on the core dimensions. The soft magnetic cores of four different magnetic materials were investigated, that is, Sendust (Kool Mμ®), Fe-Si (XFlux®), Mo-Permalloy powder cores provided from Magnetics Inc., and a MnZn ferrite core provided from TOKIN Corp., as summarized in Table 1. The relative initial permeability $\mu_i$ of the Sendust, Fe-Si, and Mo-Permalloy powder cores were 60 while that of the ferrite core was 2,900. Then, the soft magnetic cores of

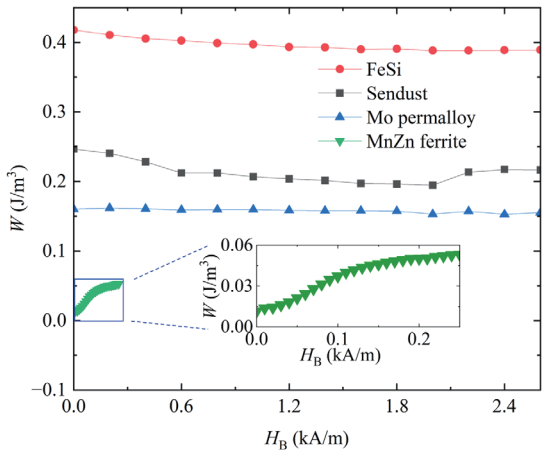


**Fig. 1** Core loss $W$ of Sendust, Fe-Si, Mo-Permalloy, and MnZn ferrite cores as function of $H_B$. Inset shows expanded graph of blue square region.

Mo-Permalloy powder cores with different $\mu_i$ as summarized in Table 2 were investigated. The values of $\mu_i$ were cited from data sheets measured at 400 Hz. PCA for the analysis on $B$-$H$ curve shape was conducted by using WAVEBASE [29), 30)]. The raw $B$-$H$ curve data measured by $B$-$H$ analyzer consisted of 8,192 data points, and it was reformed into 3,661 data points with equal spacing of magnetic flux density $B$ using linear interpolation for the PCA analysis. Since the upper and lower branches of $B$-$H$ curve exhibit similar PCA results, the upper branch $B$-$H$ curve data are representatively discussed in this paper.

## 3. Result and discussion

### 3.1 Core Loss Behaviors of Various Cores under DC Bias fields

Figure 1 shows the core loss $W$ per cycle of Sendust, Fe-Si, Mo-Permalloy, and MnZn ferrite cores shown in Table 1 as a function of DC bias field $H_B$. The maximum $H_B$ for MnZn ferrite is 0.25 kA/m due to the saturation of the core. The core loss behaviors of these cores are quite different. $W$ of Fe-Si gradually decreases with $H_B$ while that of Sendust decreases initially and then slightly increases. $W$ of Mo-Permalloy remains almost unchanged. On the other hand, $W$ of MnZn ferrite significantly increases with $H_B$. Figures 2(a)-2(d) show the $B$-$H$ curves of Sendust, Fe-Si, Mo-Permalloy, and MnZn ferrite cores, respectively, with different values of $H_B$. The change in the $B$-$H$ curve shape with $H_B$ is very small for Sendust, Fe-Si, and Mo-Permalloy, as shown in Figs. 2(a)-2(c). On the other hand, the $B$-$H$ curve shape of MnZn ferrite changes from narrow lenticular to convex crescent with increasing $H_B$, as shown in Fig. 2(d). Moreover, the slope of the $B$-$H$ curve of MnZn ferrite decreases significantly. Figure 2(e) shows the effective permeability $\mu_e$ of these samples with $H_B$. $\mu_e$ of Sendust, Fe-Si, and Mo-Permalloy gradually decreases with $H_B$ while that of MnZn ferrite largely decreases even for very small $H_B$. These changes of $B$-$H$ curves were analyzed by PCA. Figures 3(a) and 3(b) exhibit the first and second principal components PC1 and PC2, respectively. Their contribution rates $p$ are 0.9995 and 0.0004, respectively, indicating that PC1 is the major contribution to the $B$-$H$ curve shape, and others are very little contributions. According to the PC1 and PC2 shown in Figs. 3(a) and 3(b), it is understood that these components represent the slope and curvature, respectively. The higher order principal components, which are not shown here, correspond to the higher order non-linearities, and their values of $p$ are even smaller [31)]. Figure 3(c) plots the component scores of PC1 and PC2, which are the normalized weight factors of PC1 and PC2, respectively. The sign of the scores has no physical meaning in this study because they are automatically given by the PCA tool. In this case, the increases in PC1 and PC2 correspond to the increases in slope and curvature, respectively. The rainbow color bar represents the value of core loss $W(0)$ at zero $H_B$, and

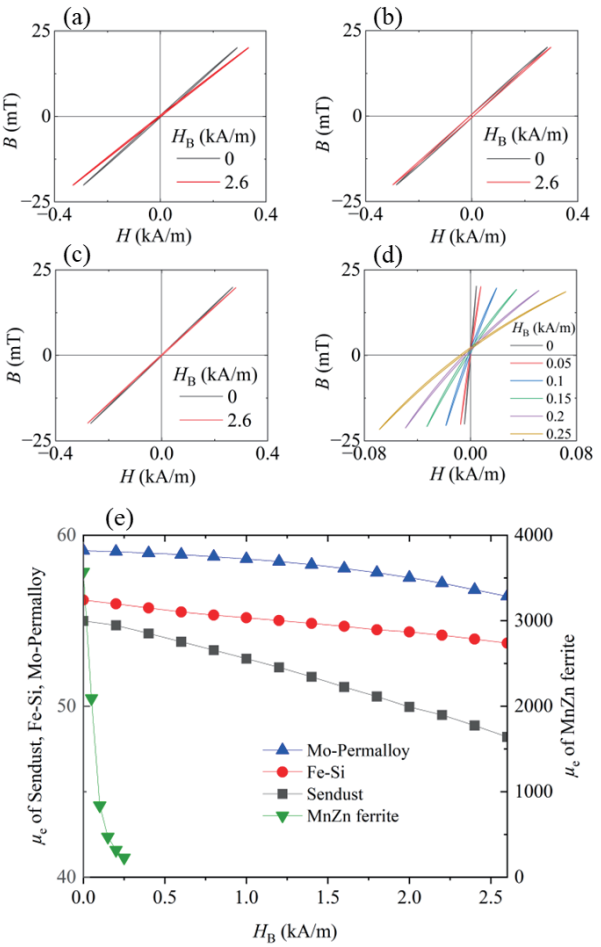


**Fig. 2** *B*-*H* curve shapes of (a) Sendust, (b) Fe-Si, (c) Mo-Permalloy, and (d) MnZn ferrite under different $H_B$. (e) Effective permeability $\mu_e$ of cores as function of $H_B$.

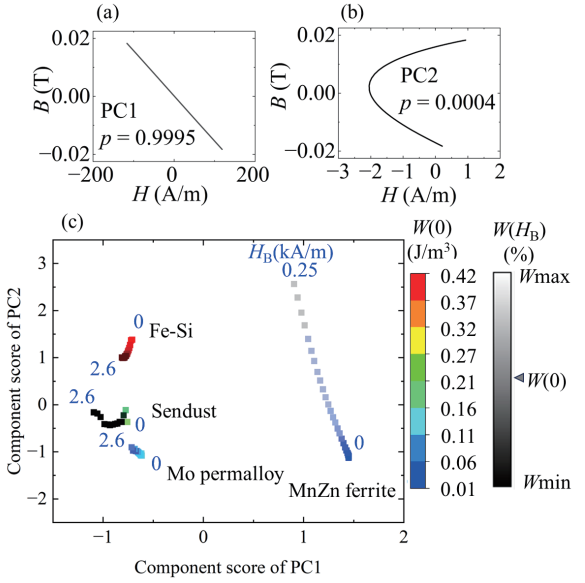


**Fig. 3** PCA analysis *B*-*H* curves of Sendust, Fe-Si, Mo-Permalloy, MnZn cores. Principal components (a) PC1 and (b) PC2 of *B*-*H* curve shape. (c) Plot of component scores of PC1 and PC2. Numbers in blue represent value of $H_B$. Rainbow color bar indicates core loss $W(0)$ at zero $H_B$, and gray-scale color bar indicates normalized core loss $W(H_B)$ with respect to $W(0)$. Values of $W$min and $W$max for Sendust, Fe-Si, and Mo-Permalloy cores are 80% and 120%, respectively, while $W$max = 500% is for MnZn ferrite core. Only $W$max is defined for MnZn ferrite core.

the gray scale color bar represents the change in the normalized core loss $W(H_B)$ with respect to $W(0)$. As shown in Fig. 3(c), the results of PCA analysis are clearly divided into two groups. One consists of the Sendust, Fe-Si, and Mo-Permalloy cores, which have $\mu_i$ of 60, and the other is the MnZn ferrite with $\mu_i$ of 2,900. The common feature of these two groups is the reduction of PC1 score with increasing $H_B$, corresponding to the reduction of the slope of *B*-*H* curve shape. This feature is well consistent with the reduction of effective permeability $\mu_e$ with increasing $H_B$, as shown in Fig. 2(e). In contrast to this common feature, there are many differences among these two groups and samples. Although the Sendust, Fe-Si, and Mo-Permalloy cores exhibit very little changes in PC2 compared with the MnZn ferrite core, their detailed behaviors of PC2 are different each other. PC2 of Fe-Si decreases with $H_B$ whereas that of Sendust core initially decreases and then increases, and that of Mo-Permalloy core slightly increases. These PC2 behaviors seem to be well consistent with the core loss behavior shown in Fig. 1. Moreover, PC2 of MnZn ferrite core largely increases with $H_B$, corresponding to the large increase in the core loss as also shown in Fig, 1. These results suggest that both PC1 and PC2 have strong relationships with the core loss behaviors even though PC2 has very little contribution to the *B*-*H* curve shape.

### 3.2 Core Loss Behaviors of Mo-Permalloy Cores with Gradually Different Permeability

In the preceding section, the results of PCA analysis of *B*-*H* curves are divided into two groups with low and high $\mu_i$ of different core materials, as shown in Fig. 3(c). In this section, we performed the PCA analysis of *B*-*H* curves of the same core material, Mo-Permalloy, with gradually different $\mu_i$ from 26 to 550, as shown in Table 2.

Figure 4 shows the core loss $W$ of Mo-Permalloy cores with gradually different $\mu_i$ with $H_B$. $W$ of the sample of $\mu_i$ = 26 decreases with increasing $H_B$, which is similar behavior of Fe-Si core as shown in Fig. 1. On the other hand, $W$ of the sample of $\mu_i$ = 60 initially decreases and then increases with $H_B$, which is similar to that of Sendust core. For the samples of $\mu_i \geq 125$, $W$ tends to increase with $H_B$, being similar to that of MnZn ferrite core. These results strongly indicate that the different behaviors of $W$ with $H_B$, which have explained as the material natures in the past, are attributed to the different values of $\mu_i$. Figures 5(a)-5(c) show the *B*-*H* curves of Mo-Permalloy cores with different $\mu_i$ of 26, 125, and 550, respectively, under various $H_B$. The *B*-*H* curve shape changes very little with $H_B$ for the sample of $\mu_i$ =

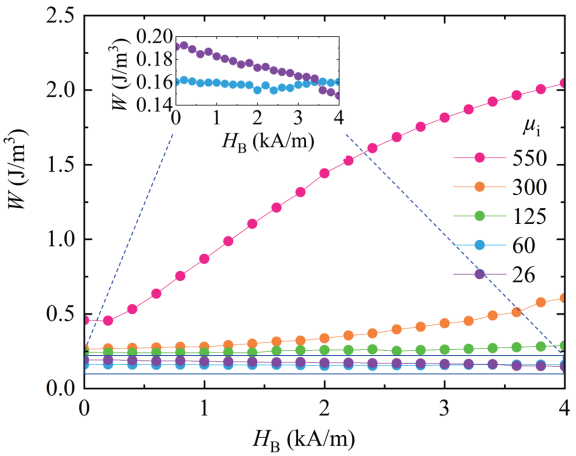


**Fig. 4** Core loss $W$ of Mo-Permalloy cores with gradually different $\mu_i$ as function of $H_B$. Inset shows expanded graph for samples with $\mu_i$ = 26 and 60.

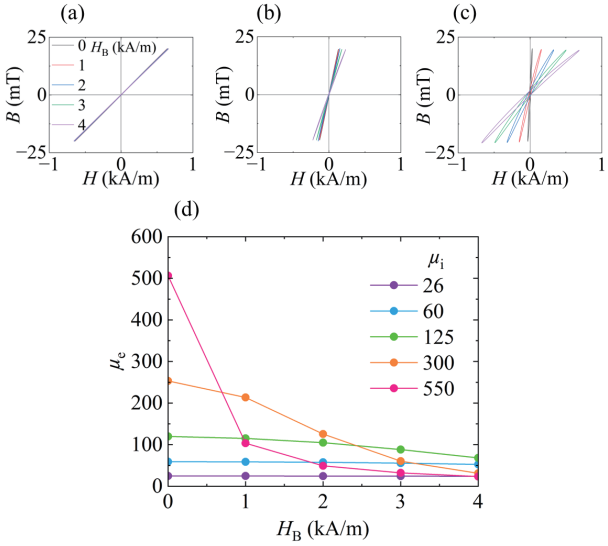


**Fig. 5** $B$-$H$ curves of Mo-Permalloy cores with (a) $\mu_i$ = 26, (b) $\mu_i$ = 125, and (c) $\mu_i$ = 550 with various $H_B$. (d) Effective permeability $\mu_e$ of these cores with gradually different $\mu_i$ as function of $H_B$.

26 whereas it changes largely for the sample of larger $\mu_i$. Figure 5(d) shows the effective permeability $\mu_e$ of these samples as a function of $H_B$. $\mu_e$ for the samples of smaller $\mu_i$ tends to be unchanged against $H_B$ whereas it for the samples of larger $\mu_i$ largely decreases with $H_B$. The PCA analysis for the $B$-$H$ curves of Mo-Permalloy cores with gradually different $\mu_i$ was performed. Figures 6(a) and 6(b) show PC1 and PC2 of the $B$-$H$ curves of Mo-Permalloy cores. As well as Figs. 3(a) and 3(b), they represent the slope and curvature, respectively. Note that the polarity of PC1 is different from that of Fig. 3(a) because of the automatic selection of the PCA tool. The contribution rates $p$ of PC1 and PC2 are 0.9920 and 0.0079, respectively. Figure 6(c) plots the component scores of PC1 and PC2, respectively. as well as Fig. 3(c).

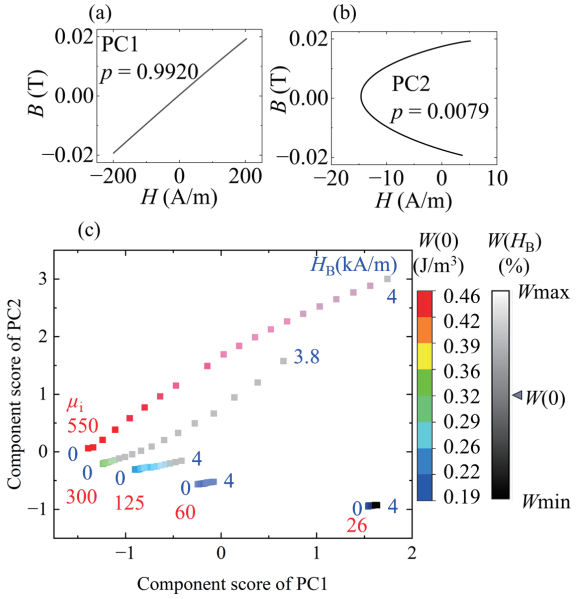


**Fig. 6** PCA analysis $B$-$H$ curves of Mo-Permalloy cores with gradually different $\mu_i$ from 26 to 550. Principal components (a) PC1 and (b) PC2 of $B$-$H$ curve shape. (c) Plot of component scores for PC1 and PC2. Numbers in red and blue represent values of $\mu_i$ and $H_B$, respectively. Rainbow color bar indicates core loss $W(0)$ at zero $H_B$, and gray-scale color bar indicates normalized core loss $W(H_B)$ with respect to $W(0)$. Values of $W$min and $W$max for samples with $\mu_i$ = 26, 60, 125, and 300 are 80% and 120%, respectively, while $W$max = 500% is for sample with $\mu_i$ = 550. Only $W$max is defined for sample with $\mu_i$ = 550.

The increases in PC1 and PC2 of Fig. 6(c) correspond to the decrease in slope and increase in the curvature, respectively. Although the PCA scores shown in Fig. 3(c) are divided into two groups, the PCA scores shown in Fig. 6(c) gradually changes with $\mu_i$. Both PC1 and PC2 scores change very little against $H_B$ for the sample of smaller $\mu_i$ whereas they largely increase for the sample of larger $\mu_i$. These results indicate that both the slope and curvature of $B$-$H$ curve are important parameters to understand the behavior of $W$ against $H_B$. The impact of slope and curvature of $B$-$H$ curve on the core loss will be discussed in the next section.

### 3.3 Discussions for Core Loss Behaviors under DC Bias Fields

To discuss the physical meanings of the changes in PC1 and PC2 scores against $H_B$, the relationship between the minor $B$-$H$ curves and the major $B$-$H$ curve of the core was studied. Figure 7(a) shows the major $B$-$H$ curves of Mo-Permalloy cores of $\mu_i$ = 26 and 550, respectively, which were measured by using $B$-$H$ analyzer at $f$ = 100 Hz. The dotted vertical line represents the applicable upper limit of $H_B$ in this study. The major $B$-$H$ curve of the sample of $\mu_i$ = 26 is almost linear below the applicable $H_B$ range whereas that of the sample of $\mu_i$ = 550 is close to be saturated. The inset of Fig. 7(a) is the expanded graph of the blue rectangle region of the major $B$-$H$ curve of the sample of $\mu_i$ = 26. The half width $H_w$ of major $B$-$H$ curve at each $H_B$, which

corresponds to coercivity for $H_B = 0$, tends to decrease with $H_B$ as shown in Fig. 7(b). This is the natural behavior of a ferromagnet sample when it is close to be saturated. Figure 7(c) shows the $B$-$H$ curves (minor curves) at various $H_B$ points on the major $B$-$H$ curves, as shown in Fig. 7(a). As observed in Fig. 6, both the PC1 and PC2 scores increase with $H_B$, corresponding the reduction in $\mu_e$ and the increase in the curvature, respectively. By comparing with the major $B$-$H$ curves, these changes in $\mu_e$ and curvature mean that the operation point of the minor $B$-$H$ curve approaches to the saturation of the major $B$-$H$ curve. In Fig. 7(b), the coercivity $H_c$ of the minor $B$-$H$ curve of the sample of $\mu_i = 26$ with $H_B$ is also plotted. $H_c$ of the minor $B$-$H$ curve is much smaller than $H_w$ of the major $B$-$H$ curve, but they both decrease with $H_B$. Thus, the reduction in $H_c$ is the factor to decrease $W$. On the other hand, the reduction in $\mu_e$ requires the larger excitation field amplitude $\Delta H$ under the condition of fixed $\Delta B$ for the core loss measurement. Thus, this factor tends to increase $W$. Therefore, the various behaviors of $W$ with $H_B$ observed in Figs. 1 and 4 would be explained by the competition between these two conflicting factors on $W$. Here, the effect of PC1, that is the slope, to $W$ is very clear as the reduction in $\mu_e$. This corresponds to the positive contribution to $W$. On the other hand, PC2, that is the curvature, reflects the degree of approaching to the saturation. Thus, the little change in PC2 score observed for the sample of smaller $\mu_i$ represents the core loss measurement far from the condition of saturation. This means that the reduction in $H_c$ which gives the negative contribution to $W$ is dominant. In contrast, the large change in PC2 observed for the sample of larger $\mu_i$ represents that the core loss measurement condition is near the saturation, resulting that the positive contribution to $W$ becomes dominant. To verify the above discussion, the components of measured core loss were evaluated. The core loss measured by using $B$-$H$ analyzer is obtained as $VA\cos\theta$ with the unit of W, where $V$ is the effective induced voltage, $A$ is the effective excitation current, and $\theta$ is the phase lag between them. Here, $\cos\theta$ is the measure corresponding to $H_c$. For the core loss measurement under fixed $\Delta B$ and fixed $f$, $W$ is proportional to the product of $A$ and $\cos\theta$. Figures 8 (a) and 8(b) show $\cos\theta$ and $A$ of all the cores used in this study as a function of $H_B$. All the cores exhibit the reduction in $\cos\theta$ and increase in $A$ with $H_B$, indicating both $H_c$ and the slope of $B$-$H$ curve decrease with $H_B$ irrespective of the value of $\mu_i$. However, the degrees of reduction in $\cos\theta$ and increase in $A$ with $H_B$ strongly depend on $\mu_i$. Figure 8(c) shows $R(A)R(\cos\theta)$, where $R(A)$ and $R(\cos\theta)$ are the ratios with respect to those values at zero $H_B$. Obviously, $R(A)R(\cos\theta)$ exhibits the similar behavior of $W$ shown in Figs. 1 and 4, that is, $R(A)R(\cos\theta)$ decreases with $H_B$ for the samples of smaller $\mu_i$ whereas it increases for the samples of larger $\mu_i$. In fact, linear relationships between $R(A)R(\cos\theta)$ and $W$ are found for all the cores irrespective of $\mu_i$ as shown in Fig. 8(d).

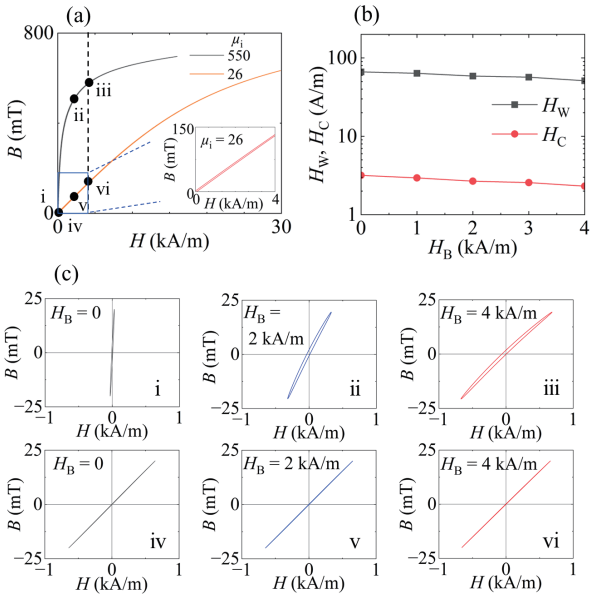


**Fig. 7** (a) Major $B$-$H$ curves of Mo-Permalloy cores with $\mu_i = 26$ and 550. Vertical dotted line corresponds to applicable upper limit of $H_B$. Inset shows expanded graph of blue rectangular region of major $B$-$H$ curve of sample with $\mu_i = 26$. (b) $H_w$ of major $B$-$H$ curve and $H_c$ of minor $B$-$H$ curve of sample with $\mu_i = 26$ as function of $H_B$. (c) Minor $B$-$H$ curves at each operation point on major $B$-$H$ curves shown in (a).

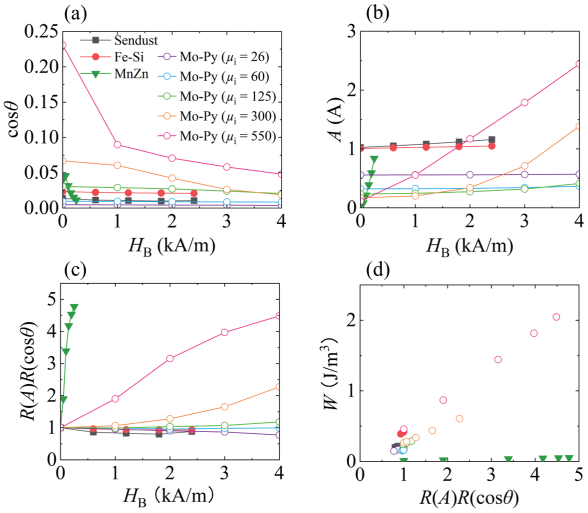


**Fig. 8** (a) $\cos\theta$, (b) $A$, and (c) $R(A)$ $R(\cos\theta)$ of all cores used in this study as function of $H_B$. (d) Relationship between $R(A)$ $R(\cos\theta)$ and core loss $W$.

## 4. Conclusion

In this study, the core loss behavior under DC bias fields were investigated through the principal component analysis of $B$-$H$ curves of various soft magnetic powder cores with different materials and different permeabilities. Different cores exhibit various core loss behaviors, which were explained as material nature in the past, exhibited very clear relationship

among the principal components of the *B*-*H* curve. As a result, these components correspond to the slope and curvature of *B*-*H* curve. Irrespective of the magnetic materials, the slope of *B*-*H* curve decreased with DC bias field, leading to the positive contribution to the core loss. On the other hand, the increase in slope corresponds to the degree of saturation. When the operation point is far from the saturation, the negative contribution to the core loss resulting from the reduction in coercivity with DC bias field becomes dominant. Therefore, as the consequence of these two conflicting positive and negative contributions determined the various core loss behaviors under the DC bias field. The important message of this work is the machine learning method effectively extracts the features of *B*-*H* curve shape which is difficult to be expressed by conventional manners, and these features greatly support to understand the various core loss behaviors under the DC bias field. In the future, the core loss prediction model instead of widely used Steinmetz equation will be constructed based on the feature extraction method.

**Acknowledgements** This work was supported by MEXT-Program for Creation of Innovative Core Technology for Power Electronics Grant Number JPJ009777 and for Data Creation and Utilization-Type Material Research and Development Project (Digital Transformation Initiative Center for Magnetic Materials) Grant Number JPMXP1122715503. WAVEBASE is supported by Toyota Motor Corporation.

## References

1) S. Busquets-Monge, J. Crebier, S. Ragon, E. Hertz, D. Boroyevich, Z. Gurdal, M. Arpilliere, and D. Lindner: *IEEE Trans. Power Electron.*, **19**, 1388, (2004).
2) B. Sarlioglu, C. T. Morris, D. Han, and S. Li: *Proc. Int. Aegean Conf. Electr. Mach. Power Electron. (ACEMP), Int. Conf. Optim. Electr. Electron. Equip. (OPTIM) Int. Symp. Adv. Electromech. Motion Syst. (ELECTROMOTION)*, 519, (2015).
3) J. Zou, N. C. Brooks, S. Coday, N. M. Ellis, and R. C. N. Pilawa-Podgurski: *Proc. IEEE 23rd Workshop Control Modeling Power Electron. (COMPEL)*, 1, (2022).
4) E. O. Prado, P. C. Bolsi, H. C. Sartori, and J. R. Pinheiro: *Energies*, **15**, 5244, (2022).
5) J. Biela, U. Badstuebner, and J. W. Kolar: *IEEE Trans. Power Electron.*, **24**, 288, (2009).
6) H. C. Sartori, J. E. Baggio, H. L. Hey, J. R. Pinheiro, and F. Beltrame: *Proc. IEEE 24th Int. Symp. Ind. Electron. (ISIE)*, 1378, (2015).
7) P. C. Bolsi, H. C. Sartori, and J. R. Pinheiro: *Proc. 13th IEEE Int. Conf. Ind. Appl. (INDUSCON)*, 1100, (2018).
8) H. C. Sartori, F. Beltrame, M. L. Martins, J. E. Baggio, and J. R. Pinheiro: *Proc. Brazilian Power Electron. Conf.*, 1304, (2013).
9) H. C. Sartori, J. E. Baggio, and J. R. Pinheiro: *Proc. 10th IEEE/IAS Int. Conf. Ind. Appl.*, 1, (2012).
10) D. Neumayr, D. Bortis, and J. W. Kolar: *CPSS Trans. Power Electron. Appl.*, **5**, 251, (2020).
11) P. V. V. Reddy, H. M. Suryawanshi, P. P. Nachankar, G. G. Talapur, and M. S. Ballal: *Int. J. Circuit Theory Appl.*, **48**, 134, (2020).
12) K. B. Ehlan, E. Akoro, H.-A. Samah, N. Kata, and A. S. Maiga: *TH Wildau Eng. Natural Sci. Proc.*, **1**, 1, (2021).
13) E. Otsuki, K. Ishii, and S. Nakano: *Proc. 25th Annu. IEEE Appl. Power Electron. Conf. Expo. (APEC)*, 74, (2010).
14) H. Kosai, Z. Turgut, and J. Scofield: *IEEE Trans. Magn.*, **49**, 4168, (2013).
15) J. Mühlethaler, J. Biela, J. W. Kolar, and A. Ecklebe: *Proc. Int. Power Electron. Conf. (ECCE ASIA)*, 2430, (2010).
16) A. Brockmeyer: *Proc. Appl. Power Electron. Conf. (APEC)*, 454, (1996).
17) M. S. Lancarotte, C. Goldemberg, and A. D. A. Penteado: *IEEE Trans. Energy Convers.*, **20**, 367, (2005).
18) C. A. Baguley, B. Carsten, and U. K. Madawala: *IEEE Trans. Magn.*, **44**, 246, (2008).
19) C. A. Baguley, U. K. Madawala, and B. Carsten: *IEEE Trans. Magn.*, **44**, 4127, (2008).
20) C. A. Baguley, U. K. Madawala, and B. Carsten: *IEEE Trans. Magn.*, **45**, 3215, (2009).
21) V. C. Valchev, A. P. Van den Bossche, and D. M. Van de Sype: *Proc. 31st Annu. Conf. IEEE Ind. Electron. Soc. (IECON)*, 837, (2005).
22) Y. Miwa and T. Shimizu: *Proc. IEEE Energy Convers. Congr. Expo. (ECCE)*, 5279, (2015).
23) H. Matsumori, T. Shimizu, K. Takano, and I. Hitoshi: *Proc. IEEE Appl. Power Electron. Conf. Expo. (APEC)*, 676, (2016).
24) H. Matsumori, T. Shimizu, T. Kosaka, and N. Matsui: *Proc. IEEE Energy Convers. Congr. Expo. (ECCE)*, 2315, (2019).
25) Y. Miwa, T. Shimizu, K. Takano, and H. Ishii: *IEEJ J. Ind. Appl.*, **8**, 57, (2019).
26) M. J. Mauger, X. Zheng, P. Kandula, and D. Divan: *Proc. IEEE Appl. Power Electron. Conf. Expo. (APEC)*, 1, (2020).
27) S. M. Holland: Principal components analysis (PCA), Dept. Geol., Univ. Georgia, Athens, GA, USA, (2008).
28) L. I. Smith: A Tutorial on Principal Components Analysis, Ithaca, NY, USA: Cornell Univ., (2002).
29) https://www.toyota.co.jp/wavebase/ (2022). [in Japanese]
30) A. Kato, M. Yano, N. Sakuma, A. Kinoshita, T. Yamaguchi, K. Danno and T. Shoji: *Materia Jpn.*, **60**, 57, (2021). [in Japanese]
31) T. Onuma, Z. Li and S. Okamoto: *IEEE Trans. Magn.*, **59**, 1, (2023).

**Received Sep. 18, 2024; Accepted Nov. 19, 2024**

## Editorial Committee Members・Paper Committee Members

S. Yabukami and T. Taniyama (Chairperson), N. H. Pham, D. Oyama and M. Ohtake (Secretary)

| | | | | | |
|---|---|---|---|---|---|
| H. Aoki | M. Goto | T. Goto | K. Hioki | S. Inui | K. Ito |
| M. Iwai | Y. Kamihara | H. Kikuchi | T. Kojima | H. Kura | A. Kuwahata |
| K. Masuda | Y. Nakamura | K. Nishijima | T. Nozaki | T. Sato | E. Shikoh |
| T. Suetsuna | K. Suzuki | Y. Takamura | K. Tham | T. Tanaka | M. Toko |
| N. Wakiya | S. Yakata | A. Yao | S. Yamada | M. Yoshida | |
| N. Adachi | K. Bessho | M. Doi | T. Doi | T. Hasegawa | R. Hashimoto |
| S. Haku | S. Honda | S. Isogami | T. Kawaguchi | T. Kawai | N. Kikuchi |
| K. Kobayashi | T. Maki | S. Muroga | M. Naoe | T. Narita | M. Sakakibara |
| Y. Sato | S. Seino | M. Sekino | Y. Shiota | T. Shirokura | S. Sugahara |
| I. Tagawa | K. Tajima | M. Takezawa | T. Takura | S. Tamaru | T. Yamazaki |
| T. Yoshida | S. Yoshimura | | | | |


## Notice for Photocopying

If you wish to photocopy any work of this publication, you have to get permission from the following organization to which licensing of copyright clearance is delegated by the copyright owner.

〈All users except those in USA〉
Japan Academic Association for Copyright Clearance, Inc. (JAACC)
6–41 Akasaka 9-chome, Minato-ku, Tokyo 107–0052 Japan
Phone 81–3–3475–5618 FAX 81–3–3475–5619 E-mail: info@jaacc.jp

〈Users in USA〉
Copyright Clearance Center, Inc.
222 Rosewood Drive, Danvers, MA01923 USA
Phone 1–978–750–8400 FAX 1–978–646–8600

If CC BY 4.0 license icon is indicated in the paper, the Magnetics Society of Japan allows anyone to reuse the papers published under the Creative Commons Attribution International License (CC BY 4.0).
Link to the Creative Commons license: http://creativecommons.org/licenses/by/4.0/
Legal codes of CC BY 4.0: http://creativecommons.org/licenses/by/4.0/legalcode


## 編集委員・論文委員

薮上 信（理事） 谷山智康（理事） Pham NamHai（幹事） 大竹 充（幹事） 小山大介（幹事）

| | | | | | | | | |
|---|---|---|---|---|---|---|---|---|
| 青木英恵 | 伊藤啓太 | 乾 成里 | 岩井守生 | 神原陽一 | 菊池弘昭 | 藏 裕彰 | 桑波田晃弘 | 小嶋隆幸 |
| 後藤太一 | 後藤 穣 | 佐藤 拓 | 仕幸英治 | 末綱倫浩 | 鈴木和也 | 高村陽太 | 田中哲郎 | 都甲 大 |
| Kim Kong Tham | | 仲村泰明 | 西島健一 | 野崎友大 | 日置敬子 | 増田啓介 | 八尾 惇 | 家形 諭 |
| 山田晋也 | 吉田征弘 | 脇谷尚樹 | | | | | | |

| | | | | | | | | |
|---|---|---|---|---|---|---|---|---|
| 安達信泰 | 磯上慎二 | 川井哲郎 | 川口昂彦 | 菊池伸明 | 小林宏一郎 | 榊原 満 | 佐藤佑樹 | 塩田陽一 |
| 白倉孝典 | 菅原 聡 | 清野智史 | 関野正樹 | 田倉哲也 | 田河育也 | 竹澤昌晃 | 田島克文 | 田丸慎吾 |
| 土井達也 | 土井正晶 | 直江正幸 | 成田正敬 | 白 怜士 | 橋本良介 | 長谷川 崇 | 別所和宏 | 本多周太 |
| 槙 智仁 | 室賀 翔 | 山崎貴大 | 吉田 敬 | 吉村 哲 | | | | |


## 複写をされる方へ

当学会は下記協会に複写複製および転載複製に係る権利委託をしています．当該利用をご希望の方は，学術著作権協会（https://www.jaacc.org/）が提供している複製利用許諾システムもしくは転載許諾システムを通じて申請ください．

権利委託先：一般社団法人学術著作権協会
〒107–0052 東京都港区赤坂9–6–41 乃木坂ビル
電話（03）3475–5618 FAX（03）3475–5619 E-mail: info@jaacc.jp

ただし，クリエイティブ・コモンズ [表示 4.0 国際] (CC BY 4.0)の表示が付されている論文を，そのライセンス条件の範囲内で再利用する場合には，本学会からの許諾を必要としません．
クリエイティブ・コモンズ・ライセンス http://creativecommons.org/licenses/by/4.0
リーガルコード http://creativecommons.org/licenses/by/4.0/legalcode.ja


**Journal of the Magnetics Society of Japan**

Vol. 49 No. 1 (通巻第337号) 2025年1月1日発行

Vol. 49 No. 1 Published Jan. 1, 2025
by the Magnetics Society of Japan
Tokyo YWCA building Rm207, 1–8–11 Kanda surugadai, Chiyoda-ku, Tokyo 101–0062
Tel. +81–3–5281–0106 Fax. +81–3–5281–0107

Printed by JPC Co., Ltd.
Sports Plaza building 401, 2–4–3, Shinkamata Ota-ku, Tokyo 144–0054
Advertising agency: Kagaku Gijutsu-sha

発行：(公社)日本磁気学会 101–0062 東京都千代田区神田駿河台 1–8–11 東京YWCA会館 207 号室
製作：ジェイピーシー 144–0054 東京都大田区新蒲田 2–4–3 スポーツプラザビル401 Tel.（03）6715–7915
広告取扱い：科学技術社 111–0052 東京都台東区柳橋 2–10–8 武田ビル 4F Tel.（03）5809–1132


Copyright ©2025 by the Magnetics Society of Japan